

ABSTRACT

KIM, DOUP. Post-growth Annealing of Lead-Free Perovskite $\text{FA}_3\text{Bi}_2\text{I}_9$ Single Crystal for Radiation Detection. (Under the direction of Dr. Ge Yang).

Lead (Pb)-based perovskite materials, such as CsPbBr_3 , MAPbI_3 ($\text{MA} = \text{CH}_3\text{NH}_3$), and MAPbBr_3 , have recently attracted a lot of attention for X-ray detector applications, due to their high stopping power, high attenuation coefficient, high resistivity, and good charge transport properties. Despite these advantages of lead-based perovskites, the use of lead poses a hazard concern to both human beings and the environment. As a solution, bismuth (Bi)-based lead-free perovskites show great potential and have been actively investigated for uses as X-ray detectors.

Here, we explored the post-growth annealing of lead-free perovskite formamidinium bismuth iodide $\text{FA}_3\text{Bi}_2\text{I}_9$ ($\text{FA} = \text{CH}(\text{NH}_2)_2$) single crystals grown by the solution method and studied the corresponding annealing effects. Among the samples annealed at different temperature, i.e., 80°C , 120°C , and 160°C , the sample annealed at 120°C represented the best optical performance, which has a reasonable bandgap energy of 1.97 eV and show clear Raman peaks. The as-fabricated $\text{Ag}/\text{FA}_3\text{Bi}_2\text{I}_9/\text{Ag}$ device using the 120°C annealed as-grown single crystal, possesses good physical properties including a high resistivity of $5.06 \times 10^{10} \Omega \text{ cm}$ and a relatively low trap density of $6.69 \times 10^8 \text{ cm}^{-3}$. Furthermore, it has achieved excellent X-ray response performance, as evidenced by a high $\mu\tau$ product of $3.39 \times 10^{-4} \text{ cm}^2 \text{ V}^{-1}$, a high sensitivity of $804 \mu\text{C Gy}_{\text{air}}^{-1} \text{ cm}^{-2}$, and an extremely low detection limit of 4.0 nGy s^{-1} . The results show that $\text{FA}_3\text{Bi}_2\text{I}_9$ single crystals can be a promising candidate material for X-ray detector applications and that post-growth annealing offers an attractive solution to improve their quality.

© Copyright 2023 by Doup Kim

All Rights Reserved

Post-growth Annealing of Lead-Free Perovskite $\text{FA}_3\text{Bi}_2\text{I}_9$ Single Crystal for Radiation Detection

by
Doup Kim

A thesis submitted to the Graduate Faculty of
North Carolina State University
in partial fulfillment of the
requirements for the degree of
Master of Science

Nuclear Engineering

Raleigh, North Carolina
2023

APPROVED BY:

Dr. Ge Yang
Committee Chair

Dr. Mohamed Bourham

Dr. Benjamin Beeler

DEDICATION

To my future LIFE.

BIOGRAPHY

Doup Kim obtained his first bachelor's degree in the Military Strategy from the Republic of Korea Air Force Academy (ROKAF) in 2013. After graduation from ROKAF, while serving as an officer in the Republic of Korea Air Force (ROKAF), he received support from the Air Force to study the Nuclear Engineering at Seoul National University starting from 2017 and obtained his second bachelor's degree in 2019. Afterwards, he served as an officer in the ROKAF again and was given an opportunity by the ROKAF to pursue a master's degree. In 2021, he started as a master student at the Department of Nuclear Engineering of North Carolina State University (NCSU).

His study for master's degree focused on developing hybrid lead-free formamidinium bismuth iodide (FA₃Bi₂I₉) perovskite single crystals for detection and imaging applications of high energy radiation, such as X-ray, gamma-ray, and alpha particle.

ACKNOWLEDGMENTS

Foremost, I would like to extend my appreciation and deep gratitude to my advisor, Dr. Ge Yang, for his invaluable teaching and support. His guidance to radiation detection material development was a great opportunity for me, and his consideration, vision, and patience provided me with motivation, inspiration, and insight for the research. He was, is, and will be a great mentor to me.

I cannot express enough thanks to Dr. Mohamed Bourham and Dr. Benjamin Beeler for serving my committee and providing their invaluable comments and feedback for my master work.

I would like to show my appreciation to the Republic of Korea Air Force (ROKAF) and Division of Civil Engineering, who provided me with an opportunity to study at North Carolina State University to pursue a master's degree.

I would like to express thanks to my colleagues, especially Dr. Da Cao and Saqr Alshogheathri, for their assistance, discussion, and support. And I would also like to express thanks to Owen Webster, Chris McRobie, and Lucia R. Gomez Hurtado for their support.

I would like to convey my appreciation to Yehee, the hesed group, worship team, and my friends in U.S for their support and pray.

Lastly, I would like to offer my heartfelt thanks to my parents for their support and love.

TABLE OF CONTENTS

LIST OF TABLES	vi
LIST OF FIGURES	vii
Chapter 1: Background and Motivation	1
1.1 Introduction.....	1
1.2 Motivation.....	4
1.3 Desired Physical Properties for Radiation Detection Materials	5
1.4 Perovskites as Radiation Detection Materials.....	9
1.4.1 Lead-Based Perovskite Materials	9
1.4.2 Lead-Free Perovskite Materials	16
1.5 Strategy to enhance the radiation detection performance	25
1.6 The Focus of This Study	25
Chapter 2: Perovskite Single Crystal Growth and Device Fabrication Method	28
2.1 Single Crystal Growth Methods.....	28
2.2 FA ₃ Bi ₂ I ₉ Single Crystal Growth	32
2.3 Temperature-Annealing of FA ₃ Bi ₂ I ₉ Single Crystal and Detector Fabrication	34
Chapter 3: Material Characterization	36
3.1 Microstructural Properties	36
3.1.1 X-ray Diffraction Pattern	36
3.1.2 Mechanical Properties.....	37
3.2 Optical Properties.....	40
3.2.1 UV-vis for Bandgap Energy	40
3.2.1 Raman Spectroscopy.....	41
3.3 Electrical Properties	45
3.3.1 Current-Voltage (I-V) Curve	45
3.3.2 Space Charge Limited Current (SCLC).....	47
Chapter 4: X-ray Response Performance	49
4.1 X-ray On/Off test	49
4.2 Mobility-Lifetime ($\mu\tau$) product and Sensitivity.....	52
4.3 Signal-to-Noise Ratio (SNR) and Detection Limit.....	55
4.4 Stability	57
4.5 X-ray Imaging.....	58
Chapter 5: Conclusion and Future Work	61
5.1 Summary and Conclusion	61
5.2 Future Work	63
REFERENCES	65
APPENDICES	80
Appendix A: Effect of Growth Seeded Solution Evaporation Growth Method	81
Appendix B: Estimation of Mobility-Lifetime ($\mu\tau$) Product	83
Appendix C: Stability under Long Time X-ray Exposure	85

LIST OF TABLES

Table 1.1	Recent results of lead-based perovskite materials for radiation detection	10
Table 1.2	Recent results of bismuth-based perovskite materials for radiation detection	18
Table 3.1	Main peaks and corresponding wavelength generated by formamidinium (FA) structure extracted from Raman spectra.	44
Table 5.1	The comprehensive radiation detection performances of pristine, 80°C, 120°C, and 160°C-annealed FA ₃ Bi ₂ I ₉ single crystal in this work	62
Table 5.2	The comparison of X-ray detection performance among the lead-free bismuth-based perovskite single crystal materials	63

LIST OF FIGURES

Figure 1.1	Dominance energy range for the interaction between radiation and the matter, i.e., photoelectric effect, Compton scattering, and pair production	2
Figure 1.2	Energy resolution of $\text{MAPbBr}_{2.94}\text{Cl}_{0.06}$ with and without guard ring. Energy resolution with and without guard ring were $3.6 \times 10^9 \Omega \text{ cm}$ and $9.7 \times 10^8 \Omega \text{ cm}$, respectively.....	11
Figure 1.3	Schematic illustration of the vertically symmetrical and vertical diode devices. One type is a symmetrical device with a Au/Single Crystal/Au structure, and the other type is an asymmetric diode device with a Ag/Single Crystal/ MoO_3 /Au structure	13
Figure 1.4	Energy-resolved spectrum of Co 57 gamma-ray source with a characteristic energy of 122 keV using a shaping time of $2 \mu\text{s}$	14
Figure 1.5	As-grown CsPbBr_3 crystals with orange color grown by the ITC method in the temperature range of $50 \sim 60 \text{ }^\circ\text{C}$	15
Figure 1.6	The photoresponse of $\text{Cs}_3\text{Bi}_2\text{I}_9$ along the [100] and [001] directions under 10 V bias, illuminated using a LED with a wavelength of 420 nm and an intensity of 10 mW cm^{-2}	19
Figure 1.7	X-ray dose rate-dependent signal-to-noise ratio (SNR) of the out-of-plane device (40 V bias). The LoD of $0.62 \text{ nGy}_{\text{air}} \text{ s}^{-1}$ is derived from the slope of the fitting line with a signal-to-noise of 3	21
Figure 1.8	Signal-to-noise ratio of the device derived by calculating the standard deviation of the X-ray photocurrent. The red dashed line represents a SNR of 3, and thus the detection limit is $59.7 \text{ nGy}_{\text{air}} \text{ s}^{-1}$ at 5 V bias, as indicated by the purple star surrounded by the red dashed circle	22
Figure 1.9	Bias-dependent photocurrent of a vertical-type device measured parallel to the (002) surface	24
Figure 1.10	Energy-dependent absorption cross-section of various materials for radiation detection, which is acquired from XCOM	27
Figure 2.1	Schematic illustration of solution-based growth method for perovskite single crystals. (a) Solution evaporation method. (b) Controlled cooling method. (c) Vapor diffusion method. (d) Mixed liquid diffusion method	29
Figure 2.2	Schematic illustration of the melt-based single crystal growth method. (a) Vertical Bridgman method. (b) Floating zone method	31

Figure 2.3	Schematic illustration of the FA ₃ Bi ₂ I ₉ single crystal growth process using seeded solution evaporation at constant temperature method and temperature annealing process using home-made annealing container	33
Figure 2.4	Comparison of as-grown crystals' surface area and thickness between from seeded method and from without seeded method	34
Figure 2.5	Schematic illustration of guard ring fabrication method for perovskite-based radiation detector device to reduce the leakage current at the edge of the device	35
Figure 3.1	Single crystal XRD patterns of as-grown and annealed FA ₃ Bi ₂ I ₉ single crystals with different annealing temperatures	37
Figure 3.2	Nanoindentation results conducted using 120°C-annealed FA ₃ Bi ₂ I ₉ single crystal at room temperature	39
Figure 3.3	Comparison of Young's modulus and hardness of pristine, 80°C-, 120°C-, and 160°C-annealed samples extracted from nanoindentation measurements.....	39
Figure 3.4	UV-vis transmission spectrum of 120°C-annealed FA ₃ Bi ₂ I ₉ single crystal at room temperature. Inset: optical bandgap derived from Tauc equation	41
Figure 3.5	Raman spectrum of 120°C-annealed FA ₃ Bi ₂ I ₉ single crystal in the Raman shift range from 50 to 300 cm ⁻¹	43
Figure 3.6	Raman spectra of pristine, 80°C-, 120°C-, and 160°C-annealed FA ₃ Bi ₂ I ₉ single crystals in the Raman shift range from 400 to 1800 cm ⁻¹ at room temperature	43
Figure 3.7	Comparison of major peak intensity between from pristine and 120°C-annealed FA ₃ Bi ₂ I ₉ single crystals	45
Figure 3.8	Home-made test box and fabricated detector device with copper plate.....	46
Figure 3.9	Dark currents versus corresponding bias voltage from -100 V to 100 V, investigated using pristine, 80°C-, 120°C-, and 160°C- annealed FA ₃ Bi ₂ I ₉ single crystals at room temperature.....	47
Figure 3.10	SCLC curve and each regions' transition point information using pristine, 80°C-, 120°C-, and 160°C-annealed FA ₃ Bi ₂ I ₉ single crystals	48
Figure 4.1	Schematic concept of X-ray response tests using Ag/FA ₃ Bi ₂ I ₉ /Ag planar detector device.....	49
Figure 4.2	X-ray induced photocurrent of Ag/FA ₃ Bi ₂ I ₉ (120°C-annealed)/Ag device under 40 V bias voltage.....	50

Figure 4.3	X-ray-dependent photocurrent of pristine, 80°C-, 120°C-, and 160°C-annealed FA ₃ Bi ₂ I ₉ single crystal.....	51
Figure 4.4	Rise time of pristine and 120°C-annealed FA ₃ Bi ₂ I ₉ single crystal under 10 V bias voltage	52
Figure 4.5	$\mu\tau$ product parameters extracted from the modified Hecht equation using charge collection efficiency (CCE).....	53
Figure 4.6	Sensitivity of 120°C-annealed FA ₃ Bi ₂ I ₉ single crystal at X-ray dose rate of 5.54 μ Gy/s under 40 V bias voltage.....	54
Figure 4.7	Comparison of $\mu\tau$ product and sensitivity from pristine, 80°C-, 120°C-, and 160°C-annealed FA ₃ Bi ₂ I ₉ single crystal	55
Figure 4.8	Comparison of X-ray dose rate-dependent SNR from pristine, 80°C-, and 120°C-annealed FA ₃ Bi ₂ I ₉ single crystal	56
Figure 4.9	Detection limit of 120°C-annealed FA ₃ Bi ₂ I ₉ single crystal using SNR data	57
Figure 4.10	Photocurrent and dark current measurement of detector device fabricated using 120°C-annealed FA ₃ Bi ₂ I ₉ single crystal every 15 days after first fabrication	58
Figure 4.11	X-ray imaging results using Ag/FA ₃ Bi ₂ I ₉ (pristine and 120°C-annealed)/Ag planar detector device from 8mm and 1.2mm lead collimator attached configuration.....	60
Figure A.1	Growth result of FA ₃ Bi ₂ I ₉ perovskite single crystals using solution evaporation method without seed.....	80
Figure A.2	Growth result of FA ₃ Bi ₂ I ₉ perovskite single crystals using solution evaporation method with seed, whose size is approximately illustrated.....	81
Figure B.1	Bias voltage dependent charge collection efficiency (CCE) estimation results of (a) pristine, (b) 80°C-, (c) 120°C-, and (d) 160°C-annealed FA ₃ Bi ₂ I ₉ as-grown single crystals.....	83
Figure C.1	Photocurrent measurement under X-ray dose rate of 6.78 Gy/s for 30 minutes using as-grown pristine and 120°C-annealed FA ₃ Bi ₂ I ₉ single crystal	84

CHAPTER 1: BACKGROUND AND MOTIVATION

This chapter explains the motivation of this study from the importance of high energy radiation detection system and perovskite materials, which have attracted much attention in the radiation detection community. After analyzing the various kinds of perovskite materials for radiation detection, the focus on this study is described.

Part of this chapter is published in *CrystEngComm* in 2022 [1].

1.1 Introduction

Advanced material technologies for detecting high energy radiation, e.g., X-rays and γ -rays, have attracted strong interest over the past few years due to their wide applications in homeland security [2][3], nuclear security [4], medical diagnosis and imaging [5][6], industrial process monitoring, non-destructive defect inspection [7], environmental survey and basic scientific research. X-rays have a relatively low energy range between around 100 eV and 100 keV, and γ -ray refers to a high energy range of around 100 keV or more. X-ray and γ -ray interact with the detector medium mainly through three mechanisms. The first mechanism is photoelectric effect, which occurs predominantly in the energy region between around 10 keV and 500 keV. When the incident radiation in this energy range reaches the detector, orbital electrons of the detector medium and the incident radiation interact, where all the energy of the incident radiation is absorbed by the orbital electrons, and as a result, the orbital electrons are emitted. In consequence, radiation can be detected by collecting signals induced by the emitted orbital electrons. The second way of interaction between incident radiation and the detector medium is through Compton scattering, which occurs dominantly in the energy range of between around 50 keV and 3 MeV. In Compton scattering, radiation transfers some energy to orbital electrons, and this energy causes orbital electrons to be scattered off. The last type of interaction is pair

production. This interaction produces a pair consisting of an electron and a positron after the collision of incident radiation with the nucleus of medium and only occurs when the incident radiation energy is above 1.022 MeV, which is the sum of the energies of the two particles [8]. The radiation energy-dependent interaction dominances are depicted in Figure 1.1 [9].

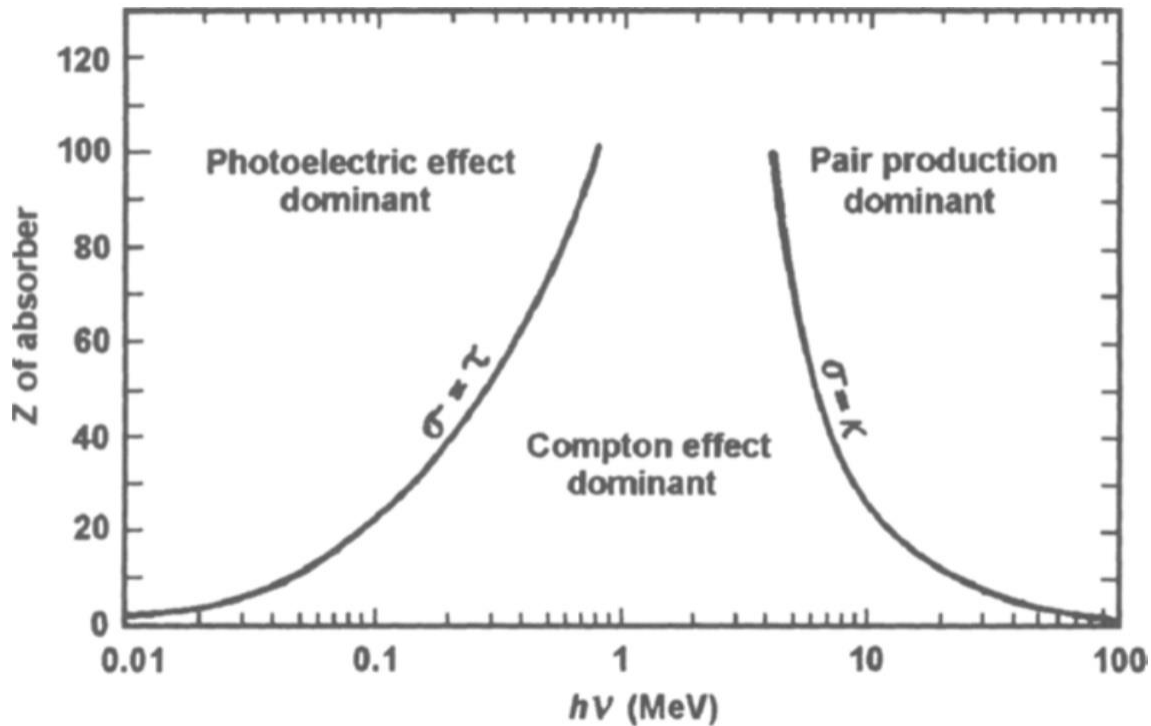


Figure 1.1 Dominance energy range for the interaction between radiation and the matter, i.e., photoelectric effect, Compton scattering, and pair production [9].

Radiation detection is often performed using either a semiconductor detector or a scintillator detector. The scintillator detects the radiation by collecting the scintillation photons generated during the scintillation process, i.e., the detector medium is first excited with the incident radiation and then de-excites to emit scintillation light. Once the scintillation photons enter the photosensors, e.g., photon multiplier tube (PMT), the light signal can be converted into an electrical signal, which is then amplified and analyzed by the readout electronics. Scintillators are generally divided into two categories: inorganic scintillators and organic scintillators. Inorganic

scintillators have high detection efficiency and show relatively good linearity for gamma-ray spectroscopy. However, large size inorganic scintillators can be very expensive to produce. Organic scintillators have the advantages of fast time response and reasonable cost when it comes to the production of large size detectors. Nevertheless, the detection efficiency of organic scintillators is generally relatively poor.

Semiconductor radiation detectors utilize electron-hole pairs generated when the incident radiation interacts with the detector medium. Compared to scintillator detectors, semiconductor detectors usually have high detection efficiency and relatively high energy resolution. Since PMT is not needed, semiconductor detectors are also less sensitive to magnetic fields. In addition, semiconductor detectors can show fast pulse rise-time and linear response over a wide energy range. All of these factors could contribute to their overall detector performance. As a classic semiconductor material, high purity Ge (HPGe) offers an extremely high energy resolution, which is well suited for gamma-ray spectroscopy application. However, HPGe detectors must work at low temperatures due to the small bandgap of Ge. Consequently, the use of HPGe detectors needs complicated cooling systems, which are often bulky and need frequent refilling of cryogen to acquire low temperature. This significantly affects their potential deployment in many practical application scenarios. To this end, room temperature semiconductor detectors are highly desired. Cadmium zinc telluride (CZT) semiconductors and its variants have been intensively studied as a leading class of room temperature radiation detector materials due to their excellent detection efficiency, high energy resolution, ambient temperature operation capability, compactness and portability, and potential for both gamma-ray spectroscopy and imaging [10][11]. Other wide bandgap semiconductors, such as gallium arsenide (GaAs), gallium nitride (GaN) and silicon carbide (SiC) have been attempted for radiation detection in harsh environment [12]. However, a

series of challenges, especially the difficulty to grow high quality detector materials at a low cost and the difficulty to process them into large-area pixelated detector matrixes [13], hinder the development of these potential radiation detector materials. To this end, it is of great significance for the community to explore new candidate detector materials for improving radiation detection capabilities to address the current issues.

1.2 Motivation

Republic of Korea (South Korea), the only divided country in the world since the Korean War from 1950 to 1953, has always been vulnerable to an attack from the Democratic People's Republic of Korea (North Korea), especially from chemical, biological, radiological, and nuclear (CBRN) threats. Radiological or nuclear weapons, are considered to pose the greatest potential damage. Therefore, it is crucial to prepare for and respond to such threats effectively, including accurately predicting the extent of damage and the affected area, and assessing the feasibility of conducting operations in the area. As the Air Force operates on the basis of a mission centered around a base, it is particularly important to anticipate the extent of damage caused by radiation. Thus, developing radiation detectors that effectively and accurately detect radiation using materials that can be applied in extreme conditions such as high or low temperature and high humidity is an important task for the South Korea Air Force.

Over the past few years, perovskite materials, which were first discovered by Russian scientist Lev Alexevich von Perovski in 1839, have exhibited exciting characteristics for a series of optoelectronic applications. The so-called 'perovskite' includes an octahedra lattice structure, and usually comes with a typical stoichiometry [14]. Besides the rapid progress of perovskites in photovoltaics [15]-[18], this class of materials has also attracted strong interest from the radiation detector community. This mainly stems from perovskite materials' unique physical properties

including high absorption coefficient, high stopping power, long carrier lifetime, high carrier mobility, and especially importantly, versatile growth approaches for low-cost manufacturing, all of which are highly appropriate for enabling radiation detection. Various forms of perovskites, e.g., films [19]-[21], wafers [22][23], nano dots/wires/plates [24], and single crystals (SCs), are being actively investigated. Among them, SC perovskites have been in the spotlight thanks to their substantially low crystal defects, which effectively contribute to the improvement of the figures of merit of the devices [25].

1.3 Desired Physical Properties for Radiation Detection Materials

For effective radiation detection, there are several requirements that detector materials must meet. High stopping power to ionizing radiation, fast response time, high sensitivity, low trap density, high carrier mobility, etc., are particularly important among these requirements.

The interaction between the incident radiation and the detector medium is an important factor towards effective radiation detection. The cross-sections (related to the probability of each interaction-) of three aforementioned interactions, have relations as follows:

- For Photoelectric Effect:

$$\tau \propto Z^{3 \text{ to } 5}$$

- For Compton scattering:

$$\sigma \propto Z$$

- For Pair Production:

$$\kappa \propto Z^2$$

where τ , σ , and κ are cross-section of Photoelectric Effect, Compton scattering, and Pair Production, respectively, and Z is an atomic number of the detector materials. Utilizing detector materials with higher Z -number means that the materials have higher possibility to interact with

the incident radiation in all energy ranges. Considering the incident radiation, such as X-rays and gamma-rays, in the energy range from 10 keV to 500 keV, the Z-number has a more critical impact on the cross-section of the interaction with detector materials, i.e., Photoelectric Effect, than other energy range of the incident gamma-rays. In this regard, high Z-number components in the detector materials contribute to a more accurate detection of the incident radiation, which elevates the quality of the radiation detectors.

Resistivity is a physical property that evaluates the conductivity of a material. Large bulk resistivity contributes to a small dark current and a low noise for a radiation detector [26][27]. The bulk crystal resistivity can be determined by measuring the current-voltage (I - V) characteristic, from which the resistivity ρ is expressed in the following way [28]:

$$\rho = \frac{R \times A}{L} = \frac{V}{I} \times \frac{A}{L}$$

where V is the voltage (V), I is the current (A), R is the resistance (Ω), L is the detector thickness, and A is the surface area (cm^2). Meanwhile, the resistivity can also be calculated using the following equation [29]:

$$\rho = \frac{m^*}{nq^2\tau}$$

where n is the carrier density, q is the carrier charge, τ is the mean free time, and m^* is the effective mass of the carriers. The requirement of resistivity for the spectroscopic semiconductor radiation detector materials should be larger than $10^9 \Omega \text{ cm}$, which guarantees a low dark current (the current obtained by applying only bias voltage, without the presence of any radiation sources) and a low noise [30]. To this end, the resistivity of detector materials is also related to both sensitivity and lower detection limit.

The mobility-lifetime ($\mu\tau$) product, which is another critical parameter of a radiation detector, accounts for the distance that the carriers can be transported per unit electric field before interaction, which is dominated by annihilation, where μ is carrier mobility (carriers' drift speed under 1 V cm^{-1}) and τ is the carriers' existence time before recombination within detector materials. As a key parameter, the $\mu\tau$ product is widely used to evaluate semiconductor detector materials' potential toward spectroscopic applications [31]. A large $\mu\tau$ product means that the charges generated through the interaction of the incident radiation with the detector medium can drift a long distance, which is often desired for achieving high radiation detector performance. The $\mu\tau$ product of the detector medium can be measured by the photoconductivity method, which is achieved by measuring the photocurrent leading to fit to the modified Hecht equation [32].

$$I = \frac{I_0 \mu \tau V}{L^2} \frac{1 - \exp\left(-\frac{L^2}{\mu \tau V}\right)}{1 + \frac{L}{V} \frac{s}{\mu}}$$

where I_0 is the saturated photocurrent, L is the thickness, s is the surface recombination velocity, and V is the applied bias. Another way to acquire the calculated $\mu\tau$ product is through the fitting of the Hecht equation using the charge collection efficiency (CCE) as in the following equation [31]:

$$CCE \approx \frac{\mu \tau V}{d^2} \cdot \left(1 - e^{-\frac{d^2}{\mu \tau V}}\right)$$

where V is the applied bias and d is a distance between the radiation sources and detector.

The sensitivity is an important requirement for high performance radiation detectors because it accounts for the efficiency of the detector material to convert the incident radiation into electrical signals, such as radiation-induced current [33]. The relationship between the sensitivity and the collected charges can be described by the following equations [34]-[36]:

$$S = \frac{Q}{AD}, (Q = \eta Q_{total})$$

where Q is the collected charges, A is the effective area of the device, D is the irradiation dose rate, and η is the charge collection efficiency. A high sensitivity radiation detector could produce more electrical signals per incident radiation photon. In this regard, many studies have been in progress to improve the sensitivity of detectors [37][38].

The detection limit is a measure of the smallest concentration which can be determined with a specified precision. Most frequently, the specified precision is defined in terms of the concentration producing a signal equivalent to three times the noise current, which can be calculated by the standard deviation of signal current [39]. Therefore, the detection limit has a close relationship with the sensitivity, which means that the lower the detection limit, the greater the ability to detect the energy of the radiation photon. As explained above, the improved $\mu\tau$ and charge collection efficiency help obtain both higher sensitivity and lower detection limits. To obtain a low detection limit, achieving a high signal with low noise is important, because the detection limit is the equivalent dose rate to produce a signal three times greater than the noise level, as defined by the International Union of Pure and Applied Chemistry (IUPAC) [39]. The detection limit is determined by finding the point where the signal-to-noise (SNR) becomes 3 or more, and the formula for calculating this SNR is as follows [40][43]:

$$SNR = \frac{I_{signal} = \bar{I}_{photo} - \bar{I}_{dark}}{I_{noise} = \sqrt{\frac{1}{N} \sum_{i=1}^N (I_i - \bar{I}_{photo})^2}}$$

where \bar{I}_{photo} and \bar{I}_{dark} represent the average photocurrent and the average dark current, respectively, and I_{noise} can be obtained by calculating the standard deviation of the photocurrent.

The energy resolution is a measure of the detectors' capability to distinguish different energies of incident radiation. It is defined by the full-width at half-maximum (FWHM) and its

corresponding energy. Literally FWHM represents the width of a peak in the spectrum, at half its maximum height, and determined by the following equation:

$$R = \frac{\Gamma}{H_0}$$

where R , Γ , and H_0 are the energy resolution, FWHM, and energy at centroid of peak spectrum, respectively [44]. Sodium iodine (NaI), one of the most common scintillators, offers an energy resolution of around 6-7% for a photon energy of 662 keV [44][45], whereas high-purity germanium (HPGe), a representative spectroscopic semiconductor detector, can provide a high energy resolution of around 0.1% for energy of 1332 keV [46].

1.4 Perovskites as Radiation Detection Materials

1.4.1 Lead-Based Perovskite Materials

Among the various perovskite families, metal halide perovskites with the general formula of ABX_3 [$A = CH_3NH_3$ (= MA, methylammonium), $CH(NH_2)_2$ (= FA, formamidinium), and Cs; $B = Pb, Bi, \text{ and } Sn$; and $X = I, Br, \text{ and } Cl$] have been actively investigated due to their remarkable performance and their facile synthesis methods [47]. In this regard, lead-based perovskite materials, especially single crystals, have exhibited promising results for applications in radiation detection [48]. Different growth techniques, e.g., solution growth method [49], and the Bridgman method [50], have been attempted to growth perovskite crystals. Among them, solution growth offers significant advantages in terms of reduction of production cost, while the Bridgman method has been able to grow lead-based perovskite single crystal radiation detector with a higher energy resolution. Table 1.1 lists the results of a few recently reported lead-based perovskite materials, which are grown by the solution method or the Bridgman method. In order to compare the performance with these perovskite materials, two non-perovskite semiconductor detector materials that are widely studied are also listed for comparison.

Table 1.1: Recent Results of Lead-based Perovskite Materials for Radiation Detection

Material	Growth Method	Properties			Ref/year
		Sensitivity/bias ($\mu\text{C Gy}_{\text{air}}^{-1} \text{cm}^{-2}/\text{V}$)	μr product ($\text{cm}^2 \text{V}^{-1}$)	Detection Limit ($\text{Gy}_{\text{air}} \text{s}^{-1}$)	
MAPbI ₃	Temperature Gradient (TG)	1471.7/3.3	2.57×10^{-3}	-	[35]/2021
CsPbBr ₃	-	-	8×10^{-3}	-	[64]/2021
MAPbBr ₃	Solution	1121/45	-	-	[57]/2020
MAPbBr ₃ /MoO ₃	Solution	2552/45	-	-	[57]/2020
CsPbBr ₃	Solution	200/45	-	-	[57]/2020
CsPbBr ₃ /MoO ₃	Solution	619/45	-	-	[57]/2020
CsPbBr ₃	Solution	770/8	-	-	[48]/2020
CsPbBr ₃	Inverse Temperature Crystallization (ITC)	1256/40 895/20 622/10 398/4	$(2.5 \pm 0.2) \times 10^{-3}$	-	[38]/2020
Cs _{0.963} Rb _{0.037} PbBr ₃	Solution (Rb doping)	8097/30	7.2×10^{-4}	-	[63]/2020
Cs _{0.634} Rb _{0.366} PbBr ₃	-	241/30	1.1×10^{-4}	-	
GAMAPbI ₃	-	23000	-	16.9×10^{-9}	[55]/2019
MAPbI ₃ (c-)	Solution	986.9/-1	3.26×10^{-3}	-	[25]/2019
MAPbI ₃ (d-)	Solution	3.4/-1	1.49×10^{-3}	-	
CsPbBr ₃	Bridgman	-	h: 9.5×10^{-4} e: 4.5×10^{-4}	-	[62]/2019
CsPbBr ₃	Bridgman	-	h: 1.34×10^{-3} e: 8.77×10^{-4}	-	[61]/2018
MAPbI ₃	Solution	-	h: 8.1×10^{-4} e: 7.4×10^{-4}	-	[53]/2018
MAPbI ₃	Solution (Se doping)	0.021	10^{-3}	-	[54]/2018
MAPbBr _{2.94} Cl _{0.06}	Solution	84000	1.8×10^{-2}	7.6×10^{-9}	[52]/2017
MAPbBr ₃	Solution	322/-1	-	-	[51]/2017
MAPbBr ₃	Solution	80/-	1.2×10^{-2}	0.5×10^{-6}	[32]/2016

Note: The '-' symbol in the table indicates that the results are not provided in the reference

The first X-ray detector made of MAPbBr₃ single crystals was reported by Wei *et al.* in 2016 [32]. They studied the relationship between the dose rate and the current density, which results in the correlation. The sensitivity of MAPbBr₃ of $80 \mu\text{C Gy}_{\text{air}}^{-1} \text{cm}^{-2}$ was achieved with a

detection limit of $0.5 \times 10^{-6} Gy_{air} s^{-1}$, and a substantially high $\mu\tau$ product of $1.2 \times 10^{-2} cm^2 V^{-1}$ was observed. Wei *et al.* also reported a Si-integrated MAPbBr₃ single crystal device using a low-temperature solution-processed molecular bonding method with the assistance of brominated (3-aminopropyl)triethoxysilane (APTES), whose chemical structure is composed of octahedra [PbBr₃]⁻¹ with MA⁺ cations inside the octahedra structure [51]. Si-integrated MAPbBr₃ shows a sensitivity of $322 \mu C Gy_{air}^{-1} cm^{-2}$. Wei *et al.* also reported MAPbBr_{2.94}Cl_{0.06} grown by the low-cost solution-growth processes and they applied a guard ring electrode to reduce leakage current [52]. Their material showed good sensitivity of $8.4 \times 10^4 \mu C Gy_{air}^{-1} cm^{-2}$ under 8 keV radiation, low detection limit of $7.6 nGy_{air} s^{-1}$, high bulk resistivity of $3.6 \times 10^9 \Omega cm$, high $\mu\tau$ product of $1.8 \times 10^{-2} cm^2 V^{-1}$, and reasonable energy resolution of 6.50%, as shown in Figure 1.2 [52].

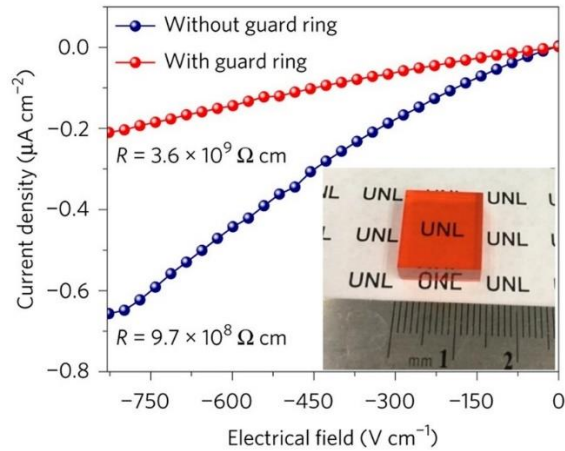


Figure 1.2 Energy resolution of MAPbBr_{2.94}Cl_{0.06} with and without guard ring. Energy resolution

with and without guard ring were $3.6 \times 10^9 \Omega cm$ and $9.7 \times 10^8 \Omega cm$, respectively [52].

He *et al.* [53] produced MAPbI₃ radiation detectors with high spectral response and low dark current for the first time with $\mu\tau$ products of up to around $\sim 0.8 \times 10^{-3} cm^2 V^{-1}$ while electron (τ_e) and hole lifetime (τ_h) are 10 μs and 17 μs , respectively. It exhibits energy resolution of 6.8%

for ^{57}Co 112 keV γ -ray and 12% for ^{241}Am 59.5 keV γ -ray. MAPbI₃ single crystal, doped with selenium (Se) during the crystallization process, resulted in fabrication of low dark current p-n junctions without any organic layers [54]. This material displayed a sensitivity of $21 \times 10^{-3} \mu\text{C Gy}_{\text{air}}^{-1} \text{cm}^{-2}$ for 59.5 keV X-ray photons (photocurrent density: 370 nA cm^{-2}) and $41 \mu\text{C Gy}_{\text{air}}^{-1} \text{cm}^{-2}$ for 1.25 MeV gamma photons. Ye *et al.* investigated MAPbI₃ grown using the concept of seed dissolution-regrowth to improve crystal quality [31]. In their study, cuboid (c-) type and dodecahedral (d-) type MAPbI₃ were fabricated and their characteristics were compared. The calculated sensitivity was $986.9 \mu\text{C Gy}_{\text{air}}^{-1} \text{cm}^{-2}$ and $\approx 3.4 \mu\text{C Gy}_{\text{air}}^{-1} \text{cm}^{-2}$ under -1 V bias for c- and d-, respectively, which was increased to $6218 \mu\text{C Gy}_{\text{air}}^{-1} \text{cm}^{-2}$ and $1045 \mu\text{C Gy}_{\text{air}}^{-1} \text{cm}^{-2}$, respectively, when increasing the bias to -13 V. Furthermore, by the relationship between photocurrent and corresponding bias voltage, the $\mu\tau$ products in the case of c- and the case of d- were $3.26 \times 10^{-3} \text{ cm}^2 \text{ V}^{-1}$ and $1.49 \times 10^{-3} \text{ cm}^2 \text{ V}^{-1}$. The cuboid type one showed better performance in sensitivity, $\mu\tau$ product, responsivity (an ability to convert the incident radiation to electrical signal) and response speed (an ability to detect the incident radiation rapidly over time) in radiation detection. By incorporating guanidinium cation (GA⁺), which improves charge collection efficiency and reduces dark current, into pristine MAPbI₃ perovskite, Huang *et al.* [55] developed GAMAPbI₃ single crystal with high sensitivity of $2.3 \times 10^4 \mu\text{C Gy}_{\text{air}}^{-1} \text{cm}^{-2}$, which is one order of magnitude increase in detector sensitivity over the state-of-the-art MAPbI₃ SCs X-ray detector ($2.5 \times 10^3 \mu\text{C Gy}_{\text{air}}^{-1} \text{cm}^{-2}$). The corresponding low detection limit of $16.9 \text{ nGy}_{\text{air}} \text{ s}^{-1}$ is improved by more than three orders of magnitude compared to the best-published result to date ($19.1 \mu\text{Gy}_{\text{air}} \text{ s}^{-1}$) [56]. As shown in Figure 1.3, Fan *et al.* [57] introduced a vertical device including a MoO₃ extraction layer, which was inserted between perovskite single crystal and Au electrode. This layer, which has a high work function, helps the

device facilitate charge transfer and enhance collection of carriers, thus leading to higher sensitivity. Au/MAPbBr₃/Au and Au/MoO₃/MAPbBr₃/Au exhibited the sensitivities of 1121 $\mu\text{C Gy}_{air}^{-1} \text{cm}^{-2}$ and 2552 $\mu\text{C Gy}_{air}^{-1} \text{cm}^{-2}$, respectively, which represents an improvement of more than two folds after adding the MoO₃ extraction layer.

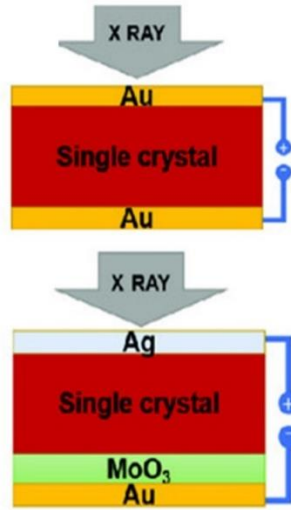


Figure 1.3 Schematic illustration of the vertically symmetrical and vertical diode devices. One type is a symmetrical device with a Au/Single Crystal/Au structure, and the other type is an asymmetric diode device a with Ag/Single Crystal/MoO₃/Au structure [57].

One of the most recent studies related to MAPbX₃ perovskite materials was made by Geng *et al.* [35]. In this study, MAPbI₃ was grown by the temperature gradient (TG) method. TG was continuously decreased in the growth process of the perovskite material, which reduced trap density, improved crystal quality, and consequently contributed to securing significantly high sensitivity. By analyzing the space-charge-limited curve (SCLC) of small TG (STG)- and large TG (LTG)-MAPbI₃ single crystals, it was confirmed that the trap density, which was calculated by using the following equation [58][59]:

$$V_{TFL} = \frac{qn_{trap}L^2}{\epsilon_0\epsilon_r}$$

where L is the sample thickness, V_{TFL} is trap-filled limit voltage, while ϵ_0 and ϵ_r are the vacuum and relative dielectric constant, respectively, was reduced to about one-tenth when STG was applied compared with the case where the LTG was applied.

Recently, all-inorganic CsPbBr_3 has emerged as a promising candidate for photodetection due to its favorable intermediate bandgap and superior photostability, thermal stability, and moisture stability [60]. Unlike the investigations related to MAPbX_3 that were mainly grown by the solution-based processes, there are quite a few studies in which CsPbX_3 was grown using the melting growth techniques, especially the Bridgman method. He *et al.* [61] reported that CsPbBr_3 single crystals grown by the Bridgman method achieved an energy resolution of 3.9% for the ^{57}Co 112 keV γ -ray and 3.8% for the ^{137}Cs 662 keV γ -ray, as shown in Figure 1.4. This material also gained high $\mu\tau$ products of $1.34 \times 10^{-3} \text{ cm}^2 \text{ V}^{-1}$ for holes and $8.77 \times 10^{-4} \text{ cm}^2 \text{ V}^{-1}$ for electrons together with long-term stability without observable significant polarization.

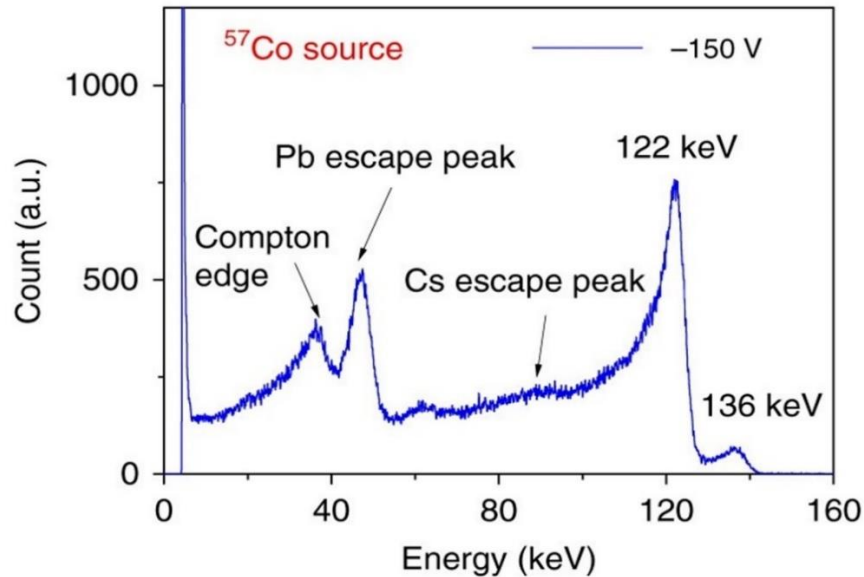


Figure 1.4 Energy-resolved spectrum of Co 57 gamma-ray source with a characteristic energy of 122 keV using a shaping time of $2 \mu\text{s}$ [61].

He *et al.* made an In/CsPbBr₃/Au Schottky type detector, which achieves a high energy resolution due to the well-controlled dark current fluctuation over time [62]. By the relationship between current density and signal acquisition time, the In/CsPbBr₃/Au detector exhibited a low dark current density of $\sim 100 \text{ nA cm}^{-2}$ under -100 V bias. Furthermore, the energy resolution of this detector was 4.8% for the ⁵⁷Co 122 keV γ -ray. The calculated $\mu\tau$ product of this detector was $9.5 \times 10^{-4} \text{ cm}^2 \text{ V}^{-1}$ for holes and $4.5 \times 10^{-4} \text{ cm}^2 \text{ V}^{-1}$ for electrons. Zhang *et al.* reported CsPbBr₃ single crystals, grown by the inverse temperature crystallization method with a sensitivity of $1256 \mu\text{C Gy}_{\text{air}}^{-1} \text{ cm}^{-2}$ under 40 V, as shown in Figure 1.5 [38].

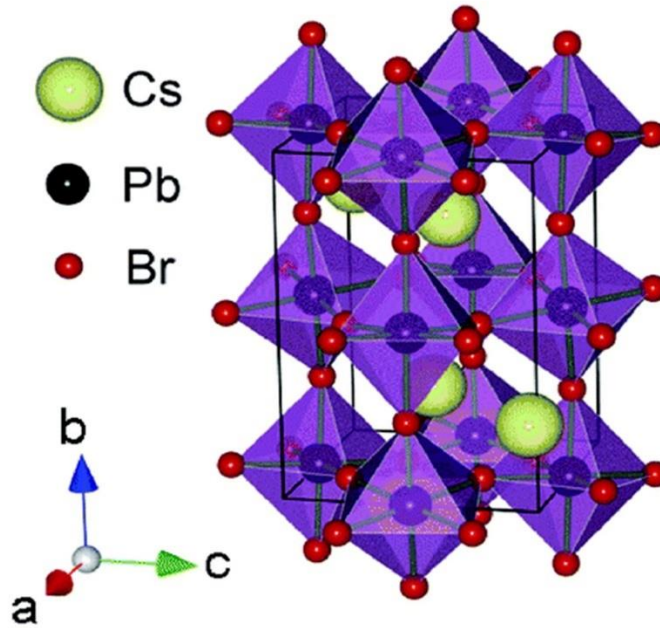


Figure 1.5 As-grown CsPbBr₃ crystals with orange color grown by the ITC method in the temperature range of 50 ~ 60 °C [38].

CsPbBr₃ material grown by the inverse temperature crystallization (ITC) was also investigated by Li *et al.* [63]. As their study showed, CsPbBr₃ single crystal doped with Rubidium (Rb) resulted in the enhancement of the atomic interaction and orbital coupling between Pb and Br atoms and contributed to an improvement of carrier transport and radiation detection performance. By

analyzing the sensitivity and its corresponding bias voltage, this inverse temperature crystallized perovskite material gained a high sensitivity of $8097 \mu\text{C Gy}_{\text{air}}^{-1} \text{cm}^{-2}$ under 30 V in the case of a small amount (0.037%) of doping, which was much higher than the case of a large amount (0.366%) of doping. This could be due to the lower trap density, the larger resistivity and the higher charge mobility in the low-doping case. Xu *et al.* reported CsPbBr₃ single crystal grown by a solution processed method [48]. In their study, a Ag/CsPbBr₃/ITO Schottky device was developed with a sensitivity of $770 \mu\text{C Gy}_{\text{air}}^{-1} \text{cm}^{-2}$ under 8 V and a low dark current density in the range of about $\sim 5 - 27 \text{ nA cm}^{-2}$ at reverse voltage. Similar with the case of MAPbBr₃, Fan *et al.* [57] demonstrated the effect of a MoO₃ extraction layer by applying the same configuration to the case of CsPbBr₃ and achieved Au/CsPbBr₃/Au and Au/MoO₃/CsPbBr₃/Au devices with the sensitivities of $200 \mu\text{C Gy}_{\text{air}}^{-1} \text{cm}^{-2}$ and $619 \mu\text{C Gy}_{\text{air}}^{-1} \text{cm}^{-2}$ under 45 V, respectively. These results indicated that adding a MoO₃ extraction layer between the perovskite single crystal and the electrodes helped increase the sensitivity of the as-fabricated radiation detectors. Recently He *et al.* reported CsPbBr₃ single crystals with a hole $\mu\tau$ product of $8 \times 10^{-3} \text{ cm}^2 \text{ V}^{-1}$ with an average value of $3.6 \times 10^{-3} \text{ cm}^2 \text{ V}^{-1}$ and a good energy resolution of 1.4% for 662 keV γ -ray [64].

1.4.2 Lead-Free Perovskite Materials

Since lead has a high Z-number of 82, the perovskites including lead could offer a high stopping power to high energy radiation. Indeed, the recent development of lead-based perovskites has demonstrated promising detector performance including high sensitivity, low detection limit, and good energy resolution. In spite of these merits, the toxicity of lead to human beings and the environment poses a main concern toward the development and deployment of lead-based perovskite-based devices [66]. As such, there is a strong interest from the radiation detector community to pursue lead-free perovskite radiation detectors. In this regard, bismuth (Bi) is

considered as a possible alternative to lead in the development of perovskites detectors. The non-toxic bismuth has a Z-number of 83 (lead: 82) and a density of 9.78g cm³ (lead: 11.34g cm³). As such it is expected that Bi-based perovskites will be able to offer high stopping power to high energy radiation as well. To this end, Bi-based double perovskite materials, which have shown a high stability and a wide bandgap energy due to their double occupancy structure [14][65], have recently received increasing attention for radiation detection. As a unique category of perovskite material system, double perovskites with a general formula of A₂M⁺M³⁺X₆, where X is halide; M⁺ and M³⁺ are monovalent and trivalent cations, respectively, have been proposed as candidate materials in the vastly expanding research field of perovskites [67][68]. Among the A₂M⁺M³⁺X₆ perovskites family, cesium silver bismuth bromide (Cs₂AgBiBr₆) has shown great potential due to its advantages of tunable band gap, high average Z-number (about 53), high resistivity, reasonable charge transport properties and facile growth approaches of bulk single crystals [69]. In addition, A₃Bi₂I₉ (A = MA, FA, and Cs) perovskite materials have also been explored as potential and attractive radiation detector materials. Table 1.2 summarizes the properties of some recently reported lead-free perovskite materials, which focus on the use of non-toxic bismuth instead of toxic lead. The classic PbI₂ and α -Se are also listed for comparison.

Table 1.2: Recent Results of Bismuth-based Perovskite Materials for Radiation detectors

Material	Growth Method	Properties				Ref/year
		Sensitivity ($\mu\text{CGy}_{\text{air}}^{-1}\text{cm}^{-2}/\text{V}$)	Resistivity (Ωcm)	$\mu\tau$ product (cm^2V^{-1})	Detection Limit ($\text{Gy}_{\text{air}}\text{s}^{-1}$)	
(BA) ₂ CsAgBiBr ₇	Solution		Pauw: $1.65 - 9.16 \times 10^{10}$ IV: 4.19×10^{11} $- 2.67 \times 10^{12}$			[58]/2021
FA ₃ Bi ₂ I ₉	Nucleation-controlled	598.1/500	7.8×10^{10}	h: 2.4×10^{-5} e: 1.3×10^{-4}	200×10^{-9}	[40]/2021
(I-BA) ₄ AgBiI ₆	Solution	5.38/60		2.28×10^{-3}		[80]/2021
MA ₃ Bi ₂ I ₉	Solution	1947/60			83×10^{-9}	[72]/2020
MA ₃ Bi ₂ I ₉	Solution	872/100	$\approx 4.7 \times 10^{10}$		31×10^{-9}	[71]/2020
MA ₃ Bi ₂ I ₉	Solution	10620/120	5.27×10^{11}	2.8×10^{-3}	0.62×10^{-9}	[73]/2020
(CPA) ₄ AgBiBr ₆	Solution	0.8/10		1.0×10^{-3}	-	[79]/2020
AgBi ₂ I ₇	Bridgman	282.5/500	1.3×10^8	h: 1.2×10^{-3} e: 3.4×10^{-3}	72×10^{-9}	[74]/2020
Cs ₃ Bi ₂ I ₉	Nucleation-controlled	1652.3/50	2.79×10^{10}	7.97×10^{-4}	130×10^{-9}	[70]/2020
Cs ₂ AgBiBr ₆	Controlled cooling	C: 1974/50 C: 677.3/20 N: 453.1/20	C: 6.10×10^9 $- 3.31 \times 10^{10}$ N: 6.04×10^7 $- 5.61 \times 10^9$		45.7×10^{-9}	[78]/2019
(BA) ₂ CsAgBiBr ₇	Solution	4.2/10	1.5×10^{11}	1.21×10^{-3}	-	[77]/2019
(PEA)Cs ₂ AgBiBr ₆	Solution	288/50	-	1.94×10^{-3}	-	[76]/2019
Cs ₂ AgBiBr ₆	Solution	165.6/50	-	9.14×10^{-4}	-	[76]/2019
Cs ₂ AgBiBr ₆	Solution	300K: 316 77K: 988	300K: 5.5×10^{11} 77K: 3.6×10^{12}		-	[75]/2018
Cs ₃ Bi ₂ I ₉	Solution		Order of 10^{10}			[29]/2018
Cs ₂ AgBiBr ₆	Solution	105/5	$10^9 - 10^{11}$	6.3×10^{-3}	59.7×10^{-9}	[39]/2017
PbI ₂	-	1200			$< 52.8 \times 10^{-9}$	[36]/2019
α -Se	-	20				[37]/2021

Note: The '-' symbol in the table indicates that the results are not provided in the reference

Among the A₃Bi₂I₉ perovskite family, high resistivity Cs₃Bi₂I₉ grown by a low temperature solution method at 50-60 °C has been reported by Zhang *et al.* [28]. The resistivity of their Cs₃Bi₂I₉ is on the order of $10^{10} \Omega\text{cm}$, as shown in Figure 1.6. In addition, the anisotropic resistivity and

the fast photoresponse along the [001] and [100] directions of $\text{Cs}_3\text{Bi}_2\text{I}_9$ were revealed in the as-fabricated coplanar and sandwich configuration devices. This is favorable for further development of $\text{Cs}_3\text{Bi}_2\text{I}_9$ in hard radiation detection. Zhang *et al.* reported that their $\text{Cs}_3\text{Bi}_2\text{I}_9$ grown by the nucleation-controlled method has a high sensitivity of $1652.3 \mu\text{C Gy}_{\text{air}}^{-1} \text{cm}^{-2}$ [70]. In addition to having a high resistivity of $2.79 \times 10^{10} \Omega \text{cm}$, this material has also a very low trap density of $1.4 \times 10^{10} \text{cm}^{-3}$, according to the SCLC curve of $\text{Cs}_3\text{Bi}_2\text{I}_9$ single crystal. In particular, this low trap density mitigated ion migration and showed a stable operation time of 13 hours. Furthermore, it showed a stable response up to a temperature of 100 °C.

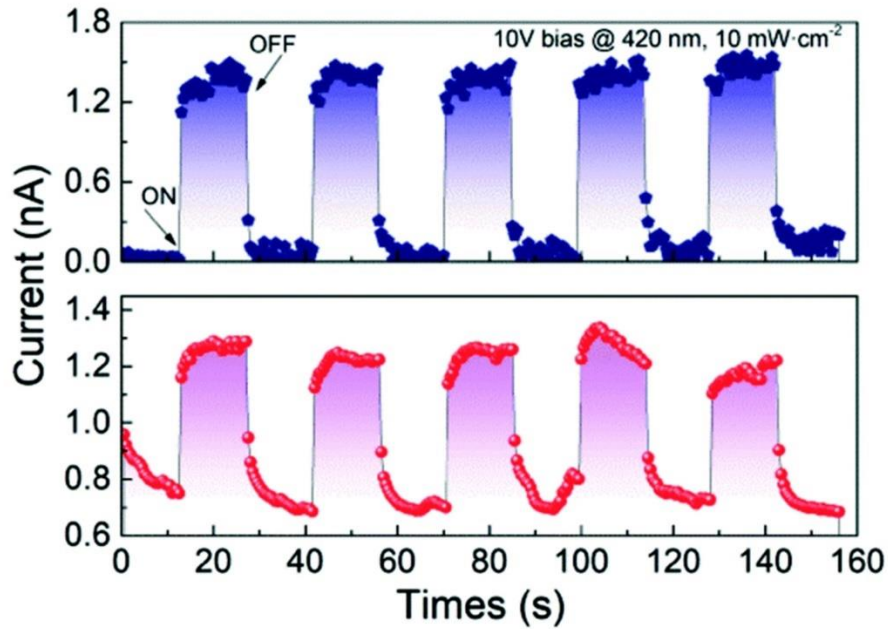


Figure 1.5 The photoresponse of $\text{Cs}_3\text{Bi}_2\text{I}_9$ along the [100] and [001] directions under 10 V bias, illuminated using a LED with a wavelength of 420 nm and an intensity of 10 mW cm^{-2} [28].

In 2020, several studies on methylammonium bismuth iodide perovskite ($\text{MA}_3\text{Bi}_2\text{I}_9$) were published within a short time frame, all of which show the results of a very high level of sensitivity. Liu *et al.* [71] investigated a $\text{MA}_3\text{Bi}_2\text{I}_9$ single crystal grown via a low-temperature solution method that achieved a sensitivity of $872 \mu\text{C Gy}_{\text{air}}^{-1} \text{cm}^{-2}$ under 100 V. They also gained a resistivity of

$\approx 4.7 \times 10^{10} \Omega \text{ cm}$, a detection limit of $31 \text{ nGy}_{\text{air}} \text{ s}^{-1}$, and a high ion migration activation energy of 0.83 eV, which contributed to the low dark current and a fast response speed of 266 μs . Besides, this material's photocurrent kept stable for about 27 hours under a total X-ray dose rate of 8270 mGy_{air} at a high bias of 100 V, while a MAPbI_3 single crystal with the same structure presented rapid decay of the current even at a much lower bias of 30 V. Liu *et al.* [72] reported inch-size zero-dimensional structured $\text{MA}_3\text{Bi}_2\text{I}_9$ single crystal grown using a precursor refinement strategy to eliminate extraneous nucleation seeds. They eventually achieved a high sensitivity of $1947 \mu\text{C Gy}_{\text{air}}^{-1} \text{ cm}^{-2}$ under 60 V, a low detection limit of $83 \text{ nGy}_{\text{air}} \text{ s}^{-1}$, and a short response time of 23.3 ms. Zheng *et al.* investigated zero-dimensional (the octahedra lattices are disconnected and located as individual units while they are sharing the corners in case of three-dimensional perovskites [14]) $\text{MA}_3\text{Bi}_2\text{I}_9$ grown by solution process, which showed the highest level of sensitivity among the studies related to lead-free perovskite materials, i.e., a sensitivity of $10620 \mu\text{C Gy}_{\text{air}}^{-1} \text{ cm}^{-2}$ under 120 V, together with high bulk resistivity of $5.27 \times 10^{11} \Omega \text{ cm}$ and high $\mu\tau$ product of $2.8 \times 10^{-3} \text{ cm}^2 \text{ V}^{-1}$ for average of hole and electron [73]. As shown in Figure 1.7, their results represent the lowest detection limit of $0.62 \text{ nGy}_{\text{air}} \text{ s}^{-1}$ among the lead-free perovskite materials investigated so far. The high ion migration energy of 0.46 eV also contributed to the low dark carrier concentration and implied the material's potential as a good radiation detector material.

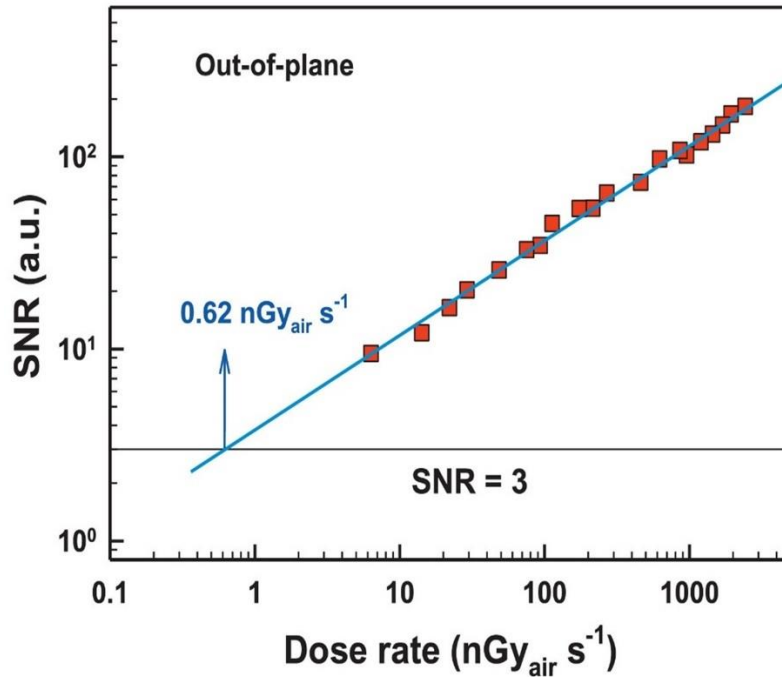


Figure 1.7 X-ray dose rate-dependent signal-to-noise ratio (SNR) of the out-of-plane device (40 V bias). The LoD of $0.62 \text{ nGy}_{\text{air}} \text{ s}^{-1}$ is derived from the slope of the fitting line with a signal-to-noise of 3 [73].

Among the most recent $\text{A}_3\text{Bi}_2\text{I}_9$ perovskite family-related research is an investigation by Li *et al.* [40], where zero-dimensional $\text{FA}_3\text{Bi}_2\text{I}_9$ single crystals with centimeter size were grown by a nucleation-controlled secondary solution constant-temperature evaporation (SSCE) method. This unique technique makes the nucleation process of the crystals more controllable, and the utilization of the precursor solution is more efficient compared to the reported ITC method. According to the bias-dependent detection efficiency curve, a high detection efficiency of 33.5% was achieved due to the high activation energy of ion conduction (E_a) of 0.56 eV. It helps ensure a relatively small dark current and low noise level under high external bias and results in the low trap density of $9.48 \times 10^9 \text{ cm}^{-3}$. Additionally, although not being exactly a part of $\text{A}_3\text{Bi}_2\text{I}_9$ perovskite family, AgBi_2I_7 single crystal grown using a vertical Bridgman method was reported by Tie *et al.* [74].

They found that AgBi_2I_7 exhibits a higher absorption coefficient over a broad photon energy range of between 1 keV and 10 MeV than many other candidate detector materials, including the currently leading room temperature semiconductor detector material CdZnTe (CZT).

Pan *et al.* explored $\text{Cs}_2\text{AgBiBr}_6$ double perovskite single crystals as an X-ray detector material [39]. They grew $\text{Cs}_2\text{AgBiBr}_6$ through a solution process and achieved a sensitivity of $105 \mu\text{C Gy}_{\text{air}}^{-1} \text{cm}^{-2}$ under 5 V and a low detection limit of $59.7 \text{ nGy}_{\text{air}} \text{ s}^{-1}$ as described in Figure 1.8. They also reported a high $\mu\tau$ product of $3.75 \times 10^{-3} \text{ cm}^2 \text{ V}^{-1}$ for the average of hole and electron, which is the highest among the results of $\text{Cs}_2\text{AgBiBr}_6$ reported so far. This outstanding performance is possibly due to the uses of post-growth thermal annealing and surface treatment, which eliminate $\text{Ag}^+/\text{Bi}^{3+}$ disordering and improve the crystal resistivity, thus resulting in the low detection limit.

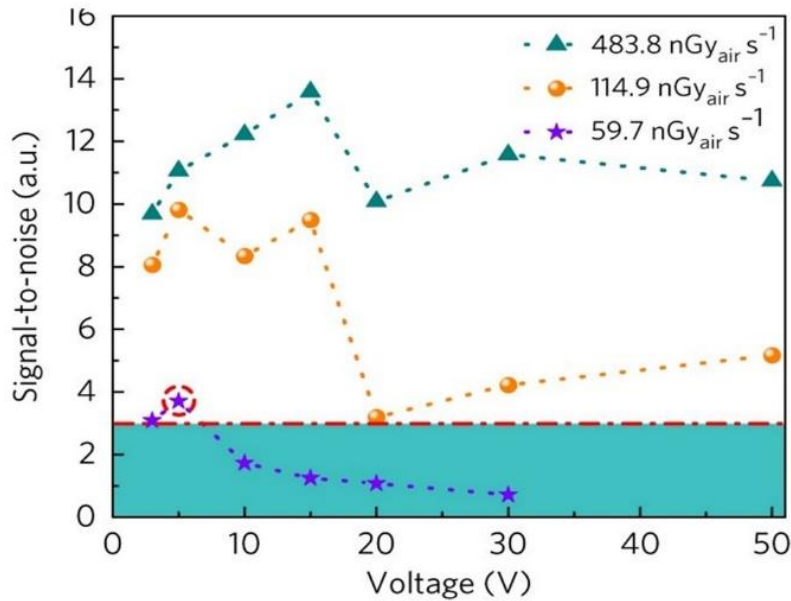


Figure 1.8 Signal-to-noise ratio of the device derived by calculating the standard deviation of the X-ray photocurrent. The red dashed line represents a SNR of 3, and thus the detection limit is $59.7 \text{ nGy}_{\text{air}} \text{ s}^{-1}$ at 5 V bias, as indicated by the purple star surrounded by the red dashed circle

[39].

Afterwards, good results corresponding to the sensitivity of $316 \mu C Gy_{air}^{-1} cm^{-2}$ for 300 K and $988 \mu C Gy_{air}^{-1} cm^{-2}$ for 77 K (liquid-nitrogen temperature) and the resistivity of $5.5 \times 10^{11} \Omega cm$ for 300 K and $3.6 \times 10^{12} \Omega cm$ for 77 K were derived by Steele *et al.* [75]. Their results indicated that the more efficient detection performance could be present at low temperatures. In 2019, Yuan *et al.* [76] innovatively introduced the phenylethylamine bromide (PEABr), which plays an important role in complexing both the Bi^{3+} and Ag^+ ions and consequently gives rise to the enhanced ordering arrangement of the Bi^{3+} and Ag^+ ions, into the $Cs_2AgBiBr_6$ perovskite precursor system. As a result, their efforts helped obtain $Cs_2AgBiBr_6$ single crystals with an improved ordering degree of $[BiX_6]^{3-}$ and $[AgX_6]^{5-}$ octahedra arrangement. The tests of as-fabricated devices show that the sensitivity was about 1.7 times higher and the $\mu\tau$ product was more than two-fold higher than pristine $Cs_2AgBiBr_6$. Xu *et al.* introduced $(BA)_2CsAgBiBr_7$, where BA is n-butylammonium, adopting a 2-dimensional multilayered motif by alloying bulk cation into the 3-dimensional cubic prototype of $Cs_2AgBiBr_6$ [77]. This material exhibited a high bulk resistivity of $1.5 \times 10^{11} \Omega cm$ according to the bias voltage-dependent current density curve, and a low trap density of $4.2 \times 10^{10} cm^{-3}$. In comparison to the as-grown crystal shape from controlled cooling and natural cooling methods, Yin *et al.* [78] grew $Cs_2AgBiBr_6$ single crystals by utilizing a controlled cooling process, which leads to a smooth surface and a relatively high resistivity with good reproducibility. In contrast, natural cooling results in rough surface with triangular and hexagon terraces. When the controlled cooling was applied, the sensitivities of $677.3 \mu C Gy_{air}^{-1} cm^{-2}$ under 20 V and $1974 \mu C Gy_{air}^{-1} cm^{-2}$ under 50 V were achieved, which is quite high considering the sensitivity of $453.1 \mu C Gy_{air}^{-1} cm^{-2}$ under 20 V when the natural cooling is applied. Through these efforts, the effectiveness of controlled cooling was demonstrated. Recently, 2-dimensional metal-halide double perovskite $(CPA)_4AgBiBr_8$ (CPA^+ = chloropropyl

ammonium) and new layered hybrid double perovskite $(\text{I-BA})_4\text{AgBiI}_8$ ($\text{I-BA}^+ = \text{I-n-butylammonium}$) were grown and investigated by Guo *et al.* [79] and Xu *et al.* [80], respectively. As shown in Figure 1.9, $(\text{CPA})_4\text{AgBiBr}_8$ exhibited a $\mu\tau$ product of $1.0 \times 10^{-3} \text{ cm}^2 \text{ V}^{-1}$ for the average of hole and electron, which is almost four orders of magnitude higher than that of MAPbI_3 film ($2 \times 10^{-7} \text{ cm}^2 \text{ V}^{-1}$) [81]. Owing to its unique crystal structure forming the AgI_6 and BiI_6 octahedral and an inorganic layer composed of the two different octahedron, $(\text{I-BA})_4\text{AgBiI}_8$ showed $\mu\tau$ product of $2.28 \times 10^{-3} \text{ cm}^2 \text{ V}^{-1}$ and low trap density of $3.78 \times 10^{10} \text{ cm}^{-3}$. The recent research on $\text{Cs}_2\text{AgBiBr}_6$ double perovskite single crystals by Murgulov *et al.* [58] focused on 2-dimensional, layered $(\text{BA})_2\text{CsAgBiBr}_7$ grown by solution process. This material gained not only a low trap density of $1.12 - 1.76 \times 10^{11} \text{ cm}^{-3}$ but also the highest resistivity, i.e., $4.19 \times 10^{11} - 2.67 \times 10^{12} \Omega \text{ cm}$ among the lead-free perovskite materials investigated so far.

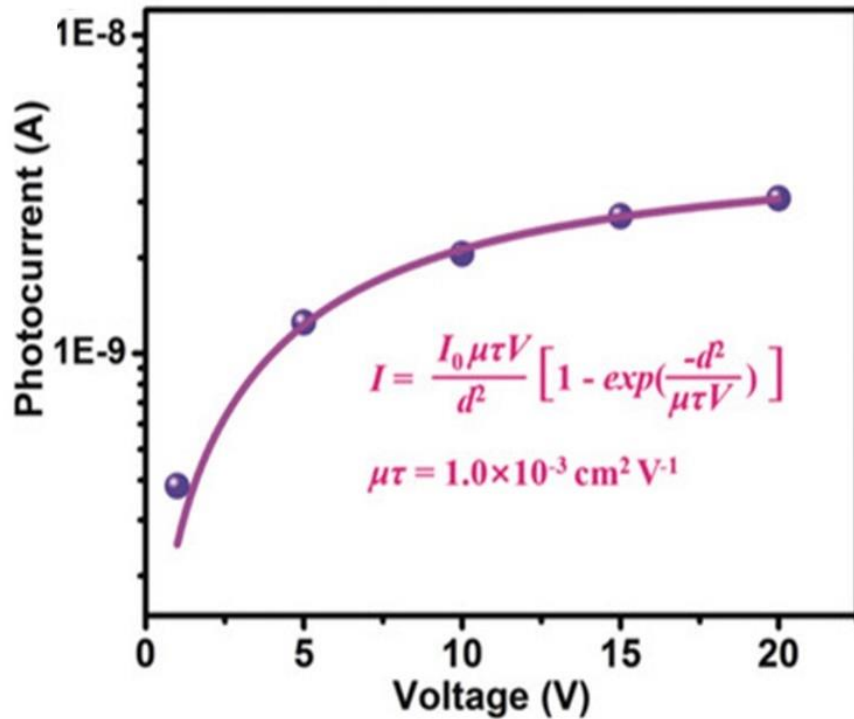


Figure 1.9 Bias-dependent photocurrent of a vertical-type device measured parallel to the (002) surface [81].

1.5 Strategy to Enhance the Radiation Detection Performance

Generally, many perovskites have suffered from ion migration, which can induce ion recombination, mitigation of charge carrier (i.e., electrons and holes) and performance instability. These kinds of ion migration-generated phenomena result in degradation of perovskite single crystal's intrinsic properties and radiation detection efficiency. There have been many efforts to suppress the perovskites' ion migration and enhance the radiation detection performance, such as doping some impurities [82], diversifying device fabrication method [52], and elaborating the crystal growth method. Among them, temperature annealing method have been considered to be the most reliable way to address the degradation of single crystal caused by ion migration [83].

By annealing under appropriate temperature, the dislocation caused by applying the bias voltage [84] is adjusted and the structure of perovskite becomes more homogeneous [85]. Additionally, surface roughness, a reason of current signal loss, can be addressed by annealing. Temperature-annealed single crystals have shown improved surface condition, which results in the reduction of vacancies between the as-grown single crystals and electrodes. Many kinds of perovskites, including FAPbBr₃ [86] and CsPbBr₃ [87] have obtained better performance compared with pristine crystals, such as high photoluminescence (PL) intensity and X-ray response properties. During the temperature annealing process, it should be noted that there should be degradation and increase of defects when the perovskites are annealed under extreme conditions, e.g., high temperatures and long annealing time.

1.6 The Focus of This Study

In this work, the development of a new type of perovskite material, formamidinium bismuth iodide perovskite (FA₃Bi₂I₉) single crystal for X-ray detector material has been introduced. FA-based perovskites have been emerging over the past few years. Several recent

studies have shown that $\text{FA}_3\text{Bi}_2\text{I}_9$ single crystals possess significant potential for opto-electronic detection. $\text{FA}_3\text{Bi}_2\text{I}_9$ single crystal was first reported by Lan *et al.* for solar cell applications [88], and by Li *et al.* for X-ray detection [40]. According to the previous works of $\text{FA}_3\text{Bi}_2\text{I}_9$ single crystals, they have much potential for radiation detection materials with appropriate bandgap, high absorption coefficient, high detection efficiency, and high sensitivity. Also, the $\text{FA}_3\text{Bi}_2\text{I}_9$ single crystal has a high absorption coefficient, which is an important factor to evaluate the quality of radiation detector materials due to the fact that the degree of radiation attenuation leads to the quality of the detection system directly. XCOM [89], which is developed by the National Institute of Standards and Technology (NIST), provides the materials' absorption properties corresponding to the incident radiation energy. Thus, analyzing the absorption properties, i.e., absorption coefficient, extracted from the XCOM database can be used to determine if the material is suitable for the radiation detection system. In Figure 1.10, the absorption coefficient of $\text{FA}_3\text{Bi}_2\text{I}_9$ single crystal and other kinds of detector materials, which were obtained from the XCOM database, were depicted. The photon energy range is set from 0.01 MeV to 1.0 MeV, where the radiation detector should be generally used. The absorption coefficient of $\text{FA}_3\text{Bi}_2\text{I}_9$ single crystal is higher than that of SiC and CdZnTe (CZT) commercialized detector materials, while it is similar to another promising hybrid lead-free perovskite $\text{MA}_3\text{Bi}_2\text{I}_9$. This information can provide $\text{FA}_3\text{Bi}_2\text{I}_9$, relatively a new kind of lead-free perovskite has a promising possibility to be used as high energy radiation, e.g., X-ray, gamma-ray, and alpha particle. However, $\text{FA}_3\text{Bi}_2\text{I}_9$ single crystals for radiation detection and related applications have seldom been reported. In this regard, we study and report optical properties, electrical properties, and X-ray response performance of $\text{FA}_3\text{Bi}_2\text{I}_9$ single crystals, which are grown by solution-based constant-temperature evaporation method coupled

with targeted annealing strategy to explore their applications as a promising class of radiation detector material.

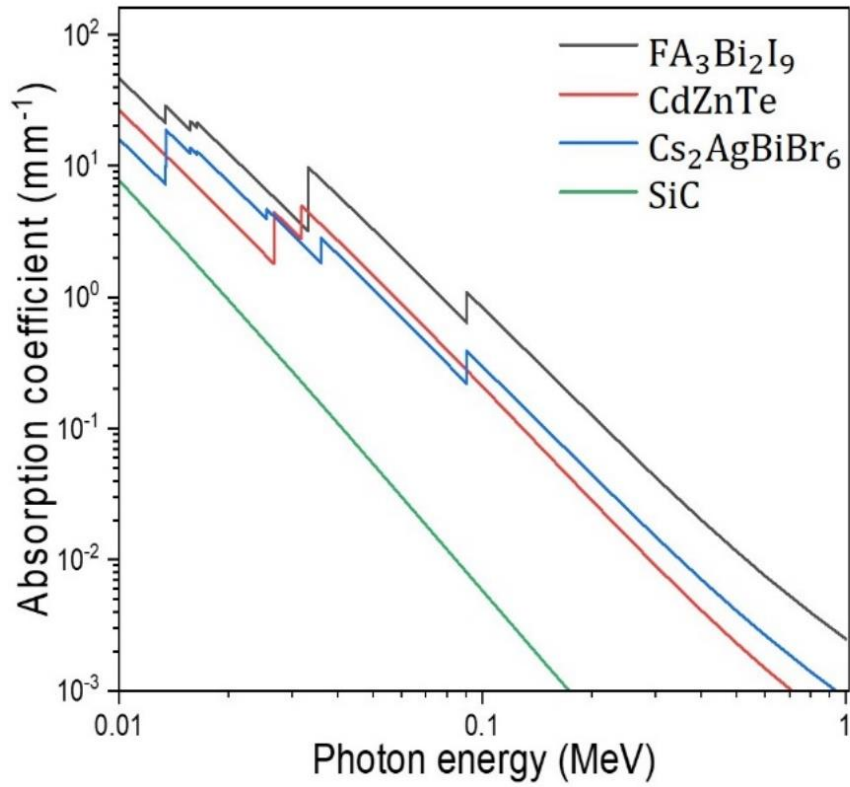


Figure 1.10 Energy-dependent absorption cross-section of various materials for radiation detection, which is acquired from XCOM.

CHAPTER 2: PEROVSKITE SINGLE CRYSTAL GROWTH AND DEVICE FABRICATION METHODS

In this chapter, the general methodologies to grow perovskite single crystals and to fabricate the detector device were introduced. From this information, the growth and fabrication methods for $\text{FA}_3\text{Bi}_2\text{I}_9$ single crystal and detector device using as-grown $\text{FA}_3\text{Bi}_2\text{I}_9$ single crystal were described, which were followed by the results of the single crystal growth and detector device fabrication.

2.1 Single Crystal Growth Methods

The growth of perovskite single crystals can be classified as two main methods, i.e., solution-based and melt-based growth methods. The solution-based method can provide various kinds of simple and effective methods, which are applied at low temperatures and in atmospheric pressure. Furthermore, the bulk size of single crystals can be obtained by using this method. Compared with the other growth methods, the solution-based method is the simplest way, which can be conducted with less growth time and no need to generate high temperature and pressure. Most importantly, it is a cost-effective method, which can be a candidate for various radiation detection applications. Figure 2.1. [90] describes four representative solution-based methods.

The solution evaporation method (Figure 2.1.(a)) can be recognized as the simplest way to generate the nucleation of single crystals, as guaranteeing the bulk sizes of single crystals. The solution, which is mixed with raw materials, is put on constant-low temperature, e.g., around higher than room temperature and lower than 100°C , so that the bulk size of single crystals can be formed at the bottom of the solution simultaneously as the solution evaporates. The controlled-cooling method (Figure 2.1.(b)) is almost the same method as the solution evaporation method except for the difference in evaporation temperature. The controlled-cooling method needs to

decrease the evaporation temperature slowly and gradually enough to keep the stable state of the solution, while the solution evaporation method maintains its evaporation temperature at as constant level through the growth procedure. The vapor diffusion method (Figure 2.1.(c)) is an effective way to generate the saturated solution by using two different solutions. The number 2 solution (outside) has a better quality than the number 1 solution (inside). The evaporate gases (vapor) of the number 1 solution go into the number 2 solution, which results in the saturation of the number 2 solution. Then the excellent quality of single crystals can be acquired at the bottom of the number 2 solution. The mixed liquid evaporation method (Figure 2.1(d)) is another powerful way to form the saturation of the solution. When two solutions with different solubilities are mixed at the intersection point, a new solution with a higher level of solubility is formed, which then triggers nucleation and allows for the growth of single crystals with good quality.

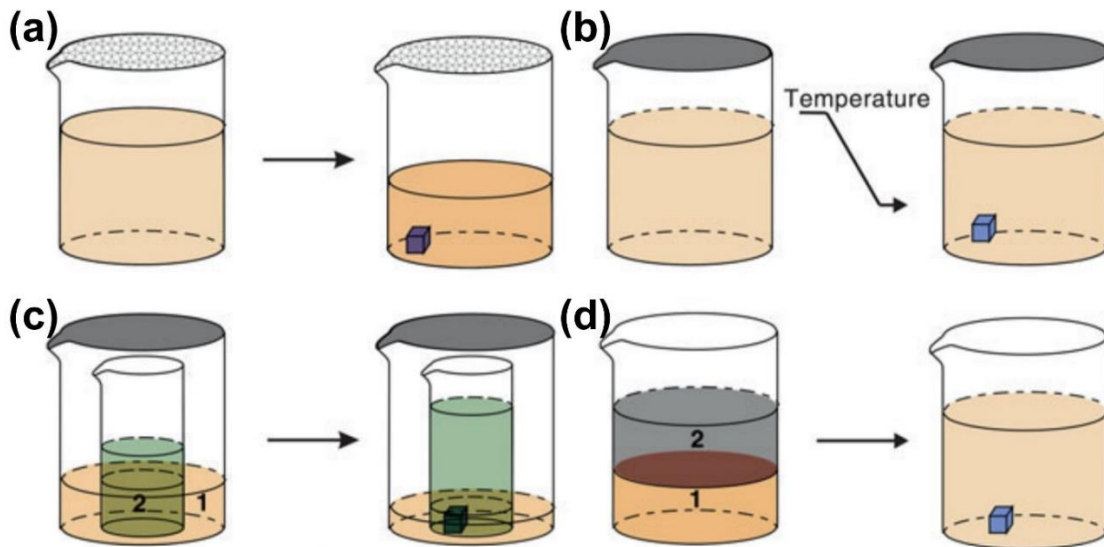


Figure 2.1 Schematic illustration of solution-based growth method for perovskite single crystals.

(a) Solution evaporation method. (b) Controlled cooling method. (c) Vapor diffusion method. (d)

Mixed liquid diffusion method [90].

The other main method for perovskite single crystal growth is melt-based method, which should be performed at high temperature. This method utilizes the procedure that the raw materials are fully melted at high temperature over the raw materials' melting point, so that the melted raw materials are coagulated to be crystalized. The single crystals grown by melt-based method generally have better purity than other types of methods, due to the reason that it has low possibility to be contaminated by the environment during the growth process. Because the growth process is done in the chamber at high temperature, which is separated by the atmosphere. Also, the bulk size of crystals can be obtained by using the melt-based method. Figure 2.2 illustrates two kinds of the melt-based perovskite single crystal growth methods [91][92].

In the case of Bridgman method (Figure 2.2.(a)), the crystal growth process involves placing the raw materials in a crucible, which is then heated to a molten state by adjusting the furnace temperature. The crucible is gradually lowered into the furnace with a specific temperature gradient to allow with the molten material to solidify directionally and form a single crystal through the process of directional solidification [91]. The floating zone method (Figure 2.2.(b)) uses a solid feed rod at the end and melt materials by high temperature generated from a halogen lamp at the other end. The feed rod slowly rotates and moves along the vertical direction, so that the bulk size of single crystal can be grown.

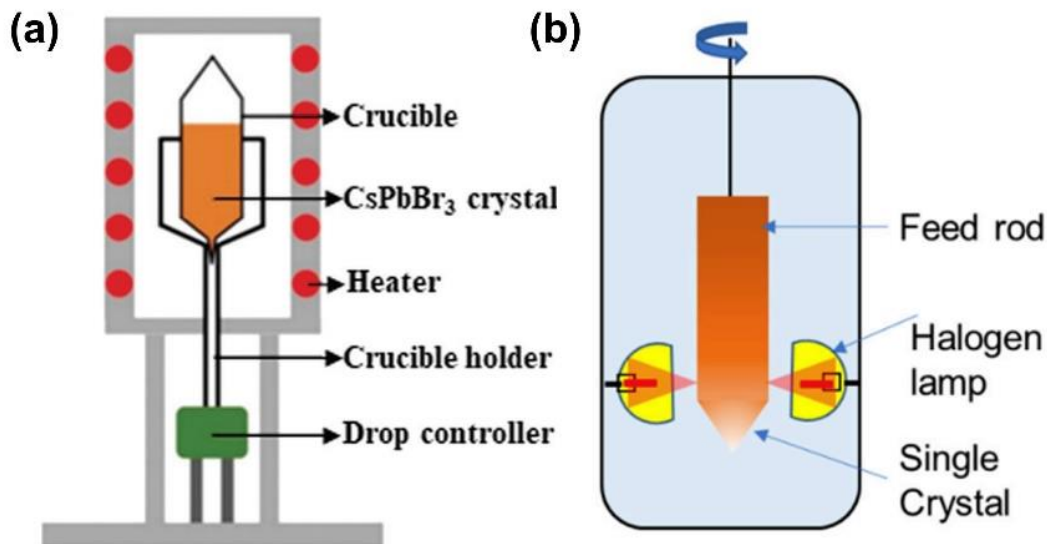


Figure 2.2 Schematic illustration of the melt-based single crystal growth method. (a) Vertical Bridgman method. (b) Floating zone method [91].

Comparing the solution-based and melt-based methods as growing a new type of hybrid lead-free perovskite, there are different advantages between the two methods. Considering the purpose of perovskite single crystal growth, the ability and possibility to be applied flexibly across various fields, e.g., homeland security, medical diagnosis, environmental remediation, and industrial inspection, is recognized as the most important aspect. To be exploited in various fields, the growth method should be simple, adjustable, and controllable, which are the advantages of the solution-based growth method.

Thus, we focused on the solution evaporation method, which is the simplest technique among the solution-based methods. Furthermore, the seeded method, which is commonly employed to grow bulk size of single crystals, is utilized to grow the perovskite single crystal, because the energy required for the nucleation is less at around the seed crystal compared with the case without any seeds. Using the seeded method, the unexpected polycrystalline is less formed and the bulk size of single crystals can be grown with the core of seed crystal.

2.2 FA₃Bi₂I₉ Single Crystal Growth

As discussed above, taking into account the purpose of developing the lead-free perovskite single crystal semiconductor for the radiation detector, the solution evaporation method can be the best method to grow the FA₃Bi₂I₉ hybrid perovskite single crystal. With the solution evaporation growth technique combined with seeded method, we can successfully obtain the bulk size of single crystal cost-effectively.

As described in Figure 2.3, the raw chemicals used for preparing FA₃Bi₂I₉ single crystals were formamidinium iodide (FAI), bismuth iodide (BiI₃), and γ -butyrolactone. 2.32 g FAI and 5.3 g BiI₃ were dissolved in 50 ml γ -butyrolactone in a glass at 60 °C and stirred for several hours followed by filtering the solution using a 0.1 μ m filter funnel. Then the filtered solution was evaporated at 75°C for 24 hours to eliminate some impurities appearing on the bottom of the glass according to the fact that the impurities can be generated easily being exposed at rapidly increased temperature. After getting rid of the impurities from the solution, the supernatant liquid was evaporated in a new glass at 55°C over several days. Then some FA₃Bi₂I₉ single crystals, which were used for seed crystals, could be formed on the bottom of the glass. The sizes of FA₃Bi₂I₉ seeds we obtained were about several millimeters in width and about less than 1 mm for thickness. Acquired seeds were put in a new glass, whose inside was filled with a new supernatant liquid obtained by the same way with seeds' case. After several days at 55°C, the bulk FA₃Bi₂I₉ single crystals were grown with the area of 140 mm² and thickness of 2.5 mm in average.

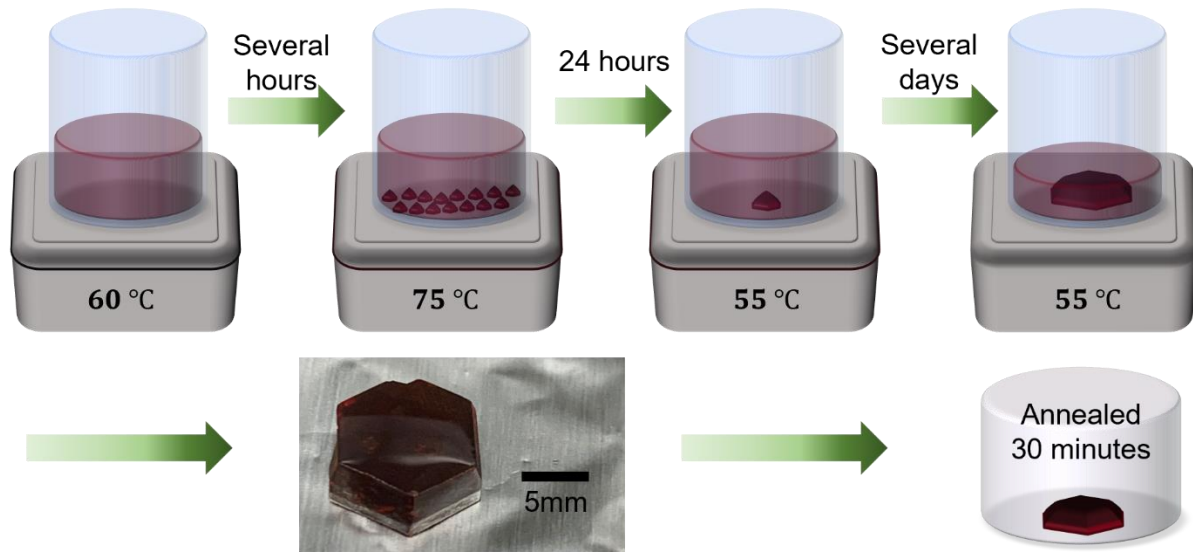


Figure 2.3 Schematic illustration of the FA₃Bi₂I₉ single crystal growth process using seeded solution evaporation at constant temperature method and temperature annealing process using home-made annealing container.

Figure 2.4 represents that the surface area of FA₃Bi₂I₉ single crystal grown by seeded method is three times bigger and the thickness is two times larger than without seeded method, which means that the seeded method can be a good option to acquire the bulk single crystal.

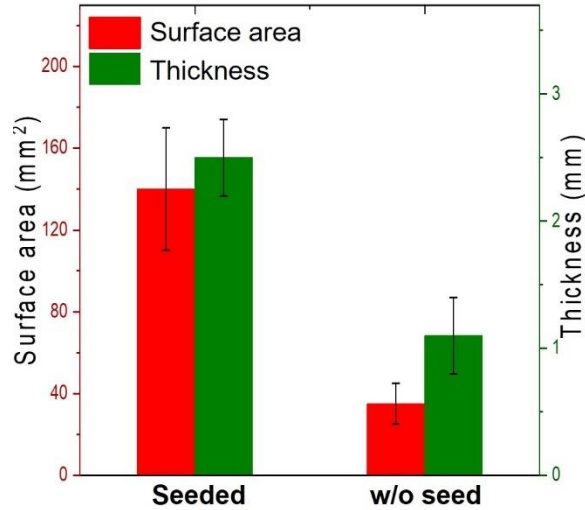


Figure 2.4 Comparison of as-grown crystals' surface area and thickness between from seeded method and from without seeded method.

2.3 Temperature-Annealing of FA₃Bi₂I₉ Single Crystal and Detector Fabrication

The as-grown crystals annealed at different temperatures, i.e., 80°C, 120°C, and 160°C, for 30 minutes in the home-made container with thermal insulators and thermocouples. By using thermal insulators, temperature leakage through the container surfaces can be mitigated. The temperature inside the container can be recognized by checking the temperature reader attached to the thermocouple. To prevent the effect of as-grown single crystal's thermal shock, the temperature was adjusted slowly and gradually, i.e., -1 °C/hour, until the temperature inside the container becomes room temperature.

The as-grown single crystals should be fabricated as detector devices to be characterized and investigated if the single crystals have suitable properties for radiation detection system. There are many kinds of ways for the as-grown single crystals to be fabricated, such as forming a guard ring to reduce the leakage current (Figure 2.5) [93], applying passivation method to enhance the charge carrier transportation [94], and employing pixel type electrodes on the surface [95]. Among the several kinds of fabrication methods, the planar detector device, which is the simplest and well-

functioning method, is selected. $\text{FA}_3\text{Bi}_2\text{I}_9$ single crystals have not been much explored yet, and post-growth temperature annealing effects on this perovskite single crystal have not been investigated. Thus, to explore $\text{FA}_3\text{Bi}_2\text{I}_9$ single crystal quality for radiation detection exactly, fabrication method should be simplified, and the performance of the detector device should be guaranteed. Planar detector devices with verified electrodes materials, i.e., gold (Au) and silver (Ag), can fulfill these requirements.

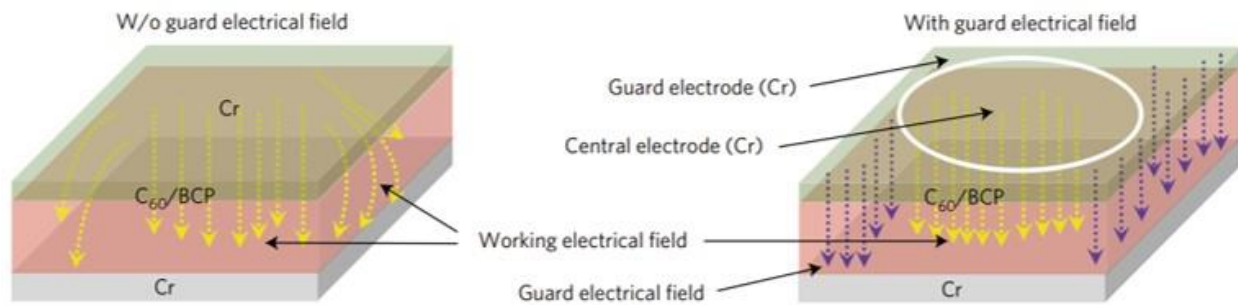


Figure 2.5 Schematic illustration of guard ring fabrication method for perovskite-based radiation detector device to reduce the leakage current at the edge of the device [93].

To fabricate the detector device using $\text{FA}_3\text{Bi}_2\text{I}_9$ single crystals, first, the $\text{FA}_3\text{Bi}_2\text{I}_9$ single crystals were polished using polishing plate with 600 and 3000 grid, so that the as-grown single crystals' surface roughness can be improved to be attached well with the electrodes. After polishing the surface, $\text{FA}_3\text{Bi}_2\text{I}_9$ single crystals were rinsed using isopropanol and toluene. Cleaning the as-grown single crystals with isopropanol and toluene helps to remove some impurities on the surface. The as-grown single crystals which have undergone both polishing and cleaning processes were ready to be fabricated as a radiation detector device. The silver (Ag) electrodes were used for fabricating the planar detector device. The fast-drying silver paste, which was purchased from Ted Pella Inc, were painted on surface of z-direction due to the reason that the $\text{FA}_3\text{Bi}_2\text{I}_9$ single crystals have intensities in the direction of (002), (004), and (006) during the X-ray diffraction (XRD) measurement. Finally, the $\text{Ag}/\text{FA}_3\text{Bi}_2\text{I}_9/\text{Ag}$ planar detector device can be fabricated.

CHAPTER 3: MATERIAL CHARACTERIZATION

To evaluate and investigate the as-grown crystal, material characterization should be processed. In this chapter, various kinds of material characterization methods are introduced, and the results of characterization are analyzed. Microstructural properties (X-ray diffraction measurements and mechanical properties), optical properties (UV-vis spectroscopy and Raman spectroscopy), and electrical properties (current-voltage curve and space-charge-limited curve) are conducted with temperature-annealed and cesium-doped $\text{FA}_3\text{Bi}_2\text{I}_9$ single crystals.

3.1 Microstructural Properties

3.1.1 X-ray Diffraction Pattern

Single crystal X-ray Diffraction (XRD) measurement can be used to investigate the single crystals' intrinsic structure so that as-grown single crystal is evaluated if it is the right and expected crystal. Also, the quality of structure can be analyzed by the single crystal XRD, because it can provide information regarding the existence of impurities or defects inside of the crystal structure. Single crystal XRD measurement was conducted by Rigaku XRD equipment at room temperature. X-rays were generated by 45 kV and 40 mA via tungsten (W) target.

As shown in Figure 3.1, for all samples, XRD results demonstrated that there are peak intensities at (002), (004), and (006) surface direction, which is same results with the previous work from Li *et al.* [40]. This indicates that the seeded solution evaporation process applied for growing $\text{FA}_3\text{Bi}_2\text{I}_9$ single crystals should guarantee to acquire high-quality of $\text{FA}_3\text{Bi}_2\text{I}_9$ single crystals. Compared with the other samples, however, 160°C-annealed crystal showed significant noise before approaching to 10 degrees and represented many secondary peaks in the range of 30 to 48 degrees and 55 to 65 degrees. According to these results, it is possible that the 160°C-annealing has introduced some damage to the crystal, leading to the degradation and

decomposition of the $\text{FA}_3\text{Bi}_2\text{I}_9$ single crystal [41][42]. This affects the radiation detection performance.

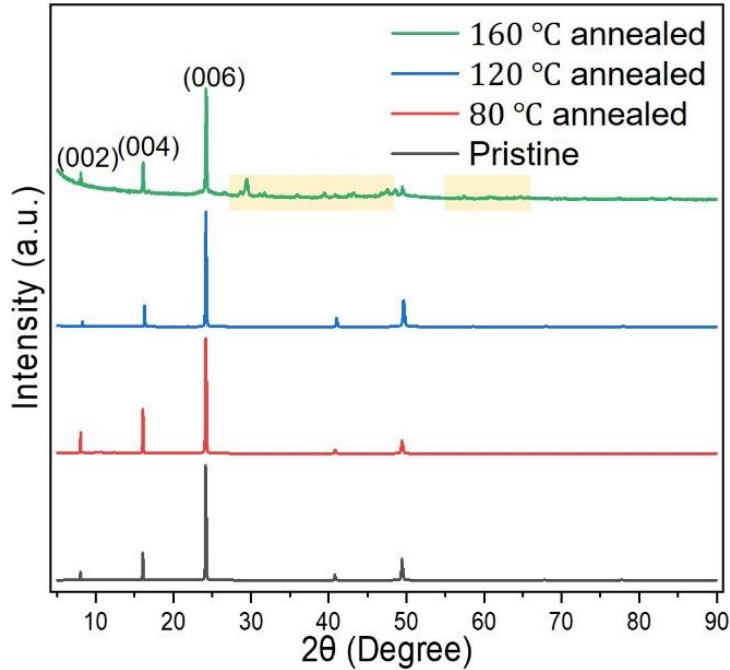


Figure 3.1 Single crystal XRD patterns of as-grown and annealed $\text{FA}_3\text{Bi}_2\text{I}_9$ single crystals with different annealing temperatures.

3.1.2 Mechanical Properties

Investigating the mechanical properties, i.e., Young's modulus and hardness, of detector materials should be an important process, due to the fact that mechanical properties can influence the materials' fabrication methods and application ranges. Young's modulus indicates the level of resistance against deformation with corresponding stress applied to the materials' surface, and hardness represents the degree of resistance to certain indentation. Both factors are the key to evaluate materials' mechanical properties. For exploring the mechanical properties, nanoindentation experiments were conducted at room temperature by a Tribo Indenter TI-980 machine. The (001) facet was selected according to the results of single crystal XRD. 5 points were selected for each samples' measurements to guarantee the reliability of the results. The

maximum loads applied for the indentation was 4 mN with 20 seconds for approaching the maximum loads, 10 seconds for holding at maximum loads, and 20 seconds for unloading to 0 mN.

The mechanical properties of $\text{FA}_3\text{Bi}_2\text{I}_9$ single crystals were investigated by nanoindentation measurements, which can most directly provide Young's modulus and hardness [96]. These two kinds of factors can be evaluated as a reliable value to test the elastic properties of the samples [97]. Among the four samples (pristine, 80°C-, 120°C-, 160°C-annealed single crystals), the 120°C-annealed single crystal showed the best results with the highest precision. Figure 3.2 illustrates the relationship between applied load and displacement of the 120°C-annealed crystal, which is the result of nanoindentation measurements at room temperature. From this data, the Young's modulus and hardness of 120°C-annealed crystal can be obtained by the Oliver-Pharr method, which is the most common method for deriving the Young's modulus and hardness of general materials [98]. As the annealing temperature increases to 120°C, the Young's modulus and hardness also increase up to a Young's modulus of 6.77 GPa and a hardness of 0.388 GPa as described in Figure 3.3. However, in the case of the 160°C-annealed crystal, both Young's modulus and hardness decrease less than the pristine crystal's value. This can be explained that 160°C-annealed crystal had some damage in the structure caused by high temperatures, which was shown with XRD measurement results.

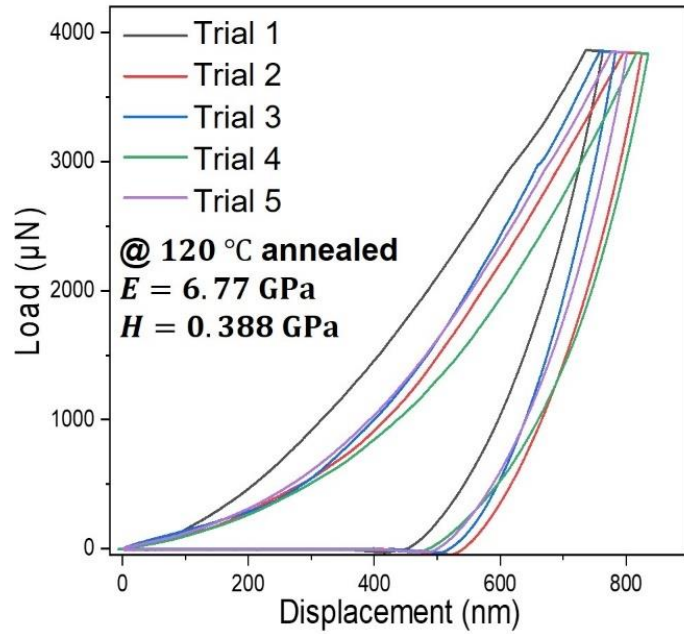


Figure 3.2 Nanoindentation results conducted using 120°C-annealed FA₃Bi₂I₉ single crystal at room temperature.

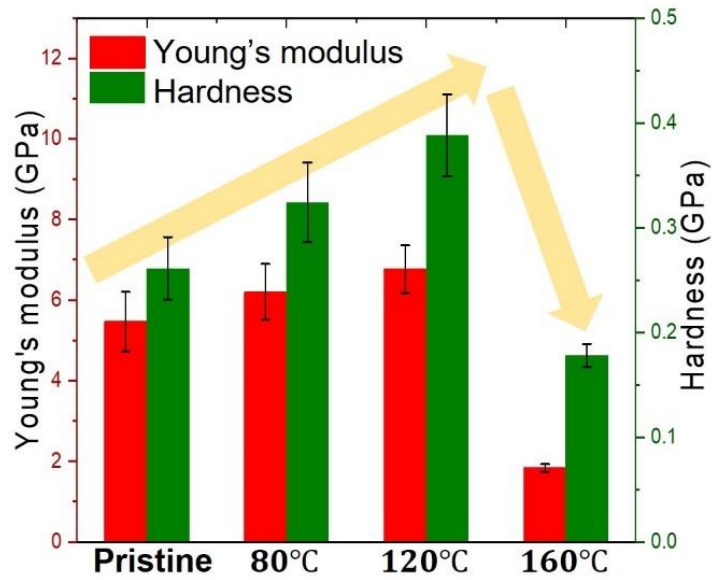


Figure 3.3 Comparison of Young's modulus and hardness of pristine, 80°C-, 120°C-, and 160°C-annealed samples extracted from nanoindentation measurements.

3.2 Optical Properties

3.2.1 UV-vis for Bandgap Energy

Ultraviolet-visible (UV-vis) measurement has been used to investigate the optical properties of materials, especially to estimate the bandgap energy of semiconductor materials. UV-vis transmission spectrum of FA₃Bi₂I₉ single crystals was obtained through a laser generated by DH-2000-BAL equipment with deuterium and halogen sources. The transmission information was recorded and acquired by Oceanview software.

Optical properties should be used to determine the single crystals' quality and verify their intrinsic characteristics. The ultraviolet-visible (UV-vis) transmission measurement for obtaining the single crystal's bandgap information. The transmission measurements of all samples of FA₃Bi₂I₉ single crystals showed the same tendency regardless of the annealing temperatures. There was, however, a difference in the level of transmission, which does not influence the estimation of the bandgap energy. As shown in Figure 3.4, the transmission data of 120°C-annealed crystal indicates that the transmission intensity increases rapidly at the wavelength of around 625 nm, which means the optical bandgap energy of FA₃Bi₂I₉ single crystal exists at around that region. Optical bandgap energy (E_g) can be derived from the Tauc equation [99]:

$$(\alpha h\nu)^{1/\gamma} = B(h\nu - E_g) \quad (1)$$

where α is the energy-dependent absorption coefficient, h is the Planck constant, ν is the frequency of photon, and B is a constant. From the inset of Figure 3.4, the derived direct bandgap energy of FA₃Bi₂I₉ single crystal semiconductor was 1.97 eV, which is in the range of semiconductors' wide bandgap energy ($> 1.7 \sim 1.8$ eV) [100] and high enough to eliminate the noise coming from room temperature and low enough to generate charge carriers, i.e., electrons and holes.

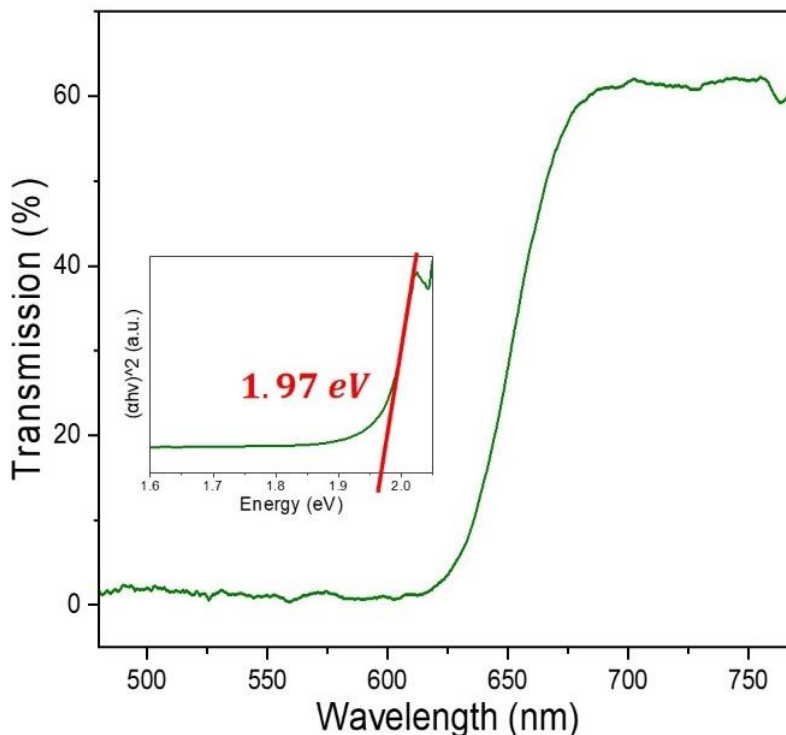


Figure 3.4 UV-vis transmission spectrum of 120°C-annealed FA₃Bi₂I₉ single crystal at room temperature. Inset: optical bandgap derived from Tauc equation.

3.2.2 Raman Spectroscopy

Raman spectroscopy, which is an excellent method to investigate the structure and chemical characteristics of materials, was conducted at room temperature using pristine, 80°C-, 120°C-, and 160°C-annealed FA₃Bi₂I₉ single crystals. For Raman spectroscopy, the Horiba XploRA PLUS was used with the grating of 1800 (450 – 850 nm), 10% filter, 100 μm slit, and 300 μm hole at room temperature, which were the optimized factors for obtaining the high resolution of peaks and minimizing the noise signals.

The optical properties of hybrid perovskites, i.e., the combination of organic and inorganic materials, can be significantly determined by the relationship between organic (FA) and inorganic (Bi and I) lattice [101]. As depicted in Figure 3.5, the Raman spectrum was obtained in the Raman shift range under 250 cm⁻¹ using 120°C-annealed crystal. There are clear Raman peaks at 63, 98,

143 cm^{-1} , which is generally analyzed as the scissoring mode from Bi-I-Bi and I-Bi-I and stretching mode from Bi-I inorganic structure, because there should be lattice vibrational motion in the relatively low Raman shift region [102]. All other samples, except the 160°C-annealed crystal, showed the same spectra in the same Raman shift range, which means that the annealing rarely changes the inorganic lattice of the $\text{FA}_3\text{Bi}_2\text{I}_9$ single crystal. In the case of 160°C-annealed crystal, the peaks were not clear and there was high level of noises. The Raman spectra of all samples in the range from 400 to 1800 cm^{-1} were described in Figure 3.6. Several kinds of major peaks can be investigated in FA ($\text{CH}(\text{NH}_2)_2$)-based perovskites. The molecular bending (δ) from NCN, torsion (τ) from NH_2 , stretching (ν) from CN, and rocking (ρ) from NH_2 are the vibrational modes, which can be found in the FA-based perovskites [103]. The bending motion (δ) is related to the change in angle of molecular bonding, which can generate the entire shape transformation, while the rocking (ρ) motion is a twisting behavior of the molecular bonding angle, which can also modify the shape of molecule. The stretching (ν) motion is related to the change of the distance between each atom. The torsion (τ) mode represents the molecules' rotational motion around the bond axis, which results in the change of dipole moment of the molecules [104]. Understanding these kinds of modes detected from Raman spectroscopy measurement is important for the perovskite materials to be applied well in various radiation detection system applications. The extracted peak positions of all samples are listed in Table 3.1.

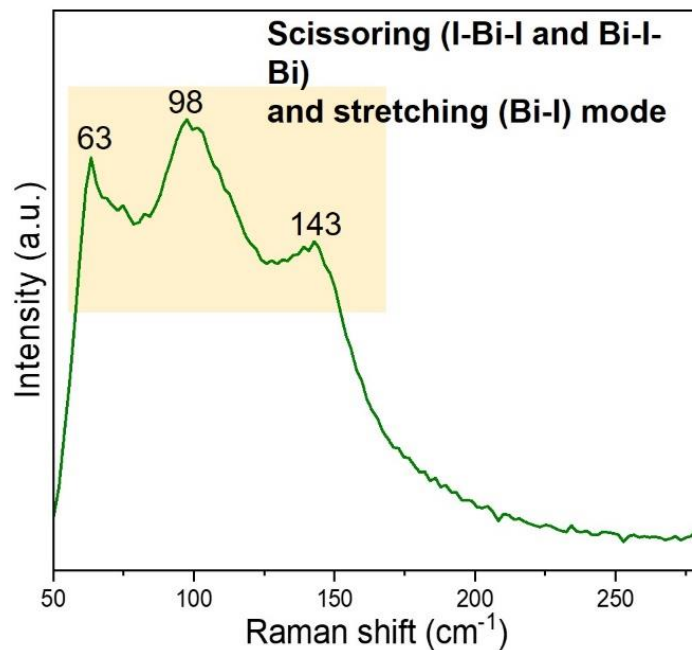


Figure 3.5 Raman spectrum of 120°C-annealed FA₃Bi₂I₉ single crystal in the Raman shift range from 50 to 300 cm⁻¹.

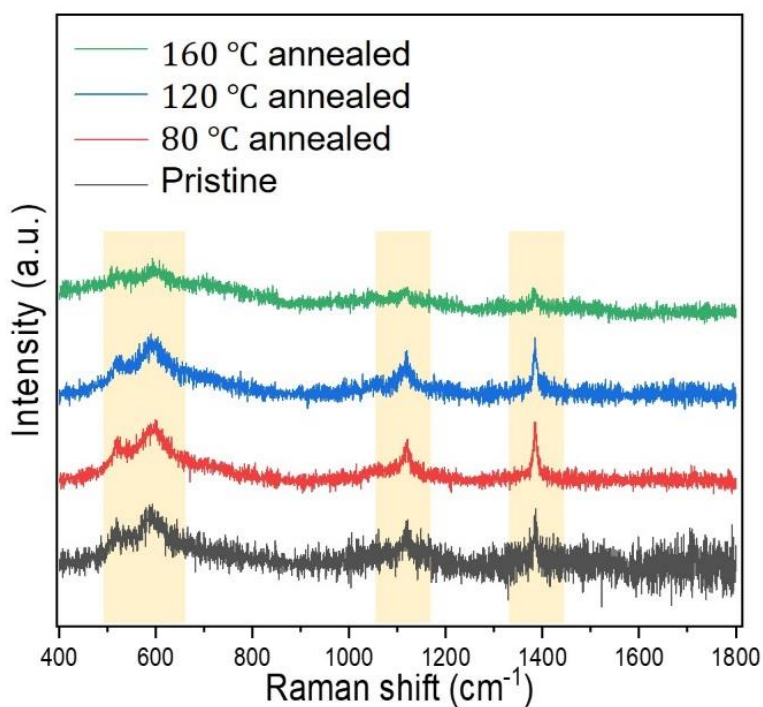


Figure 3.6 Raman spectra of pristine, 80°C-, 120°C-, and 160°C-annealed FA₃Bi₂I₉ single crystals in the Raman shift range from 400 to 1800 cm⁻¹ at room temperature.

Table 3.1 Main peaks and corresponding wavelength generated by formamidinium (FA) structure extracted from Raman spectra.

	δ (NCN)	τ (NH ₂)	ν (CN)	ρ (NH ₂)
Pristine	512	592	1121	1385
80°C annealed	514	599	1120	1385
120°C annealed	515	590	1119	1384
160°C annealed	519	593	1115	1380

The NCN bending (δ) peak was shifted to the right, which means that the bond strength can be enhanced in the bending motion of NCN as the annealing temperature increases. The peaks of CN stretching (ν) and NH₂ rocking (ρ) were shifted to the lefthand side, which means that the related bond strength can be reduced in the CN stretching mode and NH₂ rocking mode as applied temperature rises. In the case of NH₂ torsion, there is no consistent correlation among all samples, which lead to recognize the needs of further investigation in that area. For the clarity of peak, compared with the others, 160°C-annealed crystal showed relatively obscure peak intensities and more signal noises, which lead to the fact that annealing temperature 160°C can impose damages to the structure of FA₃Bi₂I₉ single crystal. Among the pristine, 80°C-, and 120°C-annealed crystals, the 120°C-annealed one demonstrated highest quality of peak intensity, as described in Figure 3.7. The signal noise of the pristine sample was denser than the 120°C-annealed sample, which provides 120°C annealed one with better Raman peak quality in all kinds of FA-based major peaks.

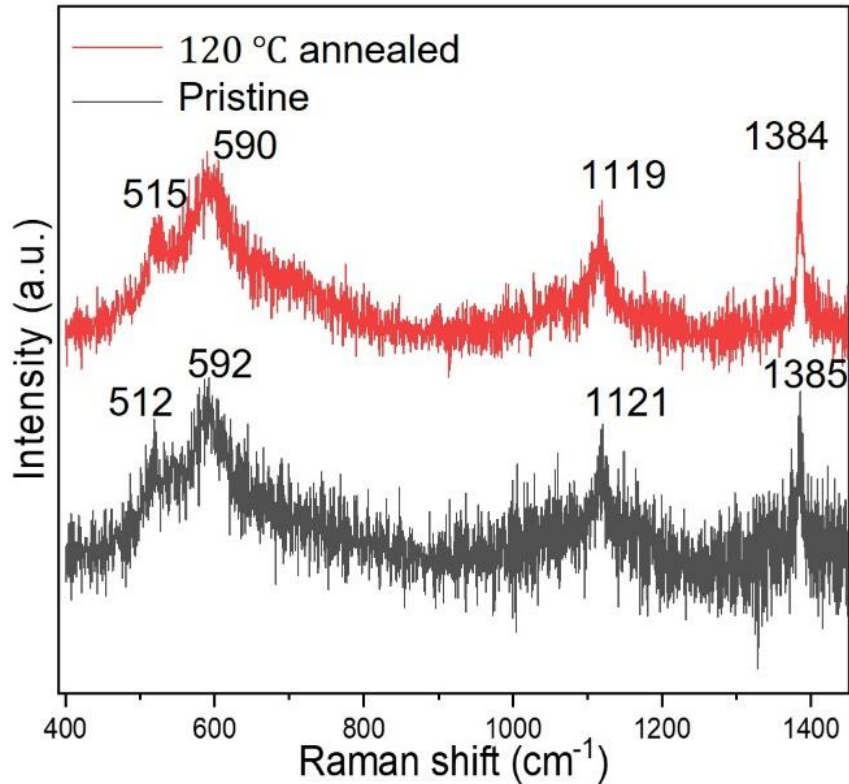


Figure 3.7 Comparison of major peak intensity between from pristine and 120°C-annealed $\text{FA}_3\text{Bi}_2\text{I}_9$ single crystals.

3.3 Electrical Properties

3.3.1 Current – Voltage (*I-V*) Curve

To investigate the electrical properties of $\text{FA}_3\text{Bi}_2\text{I}_9$ single crystal, we prepared the $\text{Ag}/\text{FA}_3\text{Bi}_2\text{I}_9/\text{Ag}$ planar detector device. As described in Figure 3.8, by using home-made electrical and X-ray response test box, which can apply bias voltage to the top of detector device and collect photocurrent signals come from the bottom of detector device, the currents generated from charge carriers inside the $\text{FA}_3\text{Bi}_2\text{I}_9$ can be collected. The detector device received the bias voltage through the copper pin and provide copper plate with generated current signals, which were transported to Keithley 6487 to obtain the current-bias voltage curve.

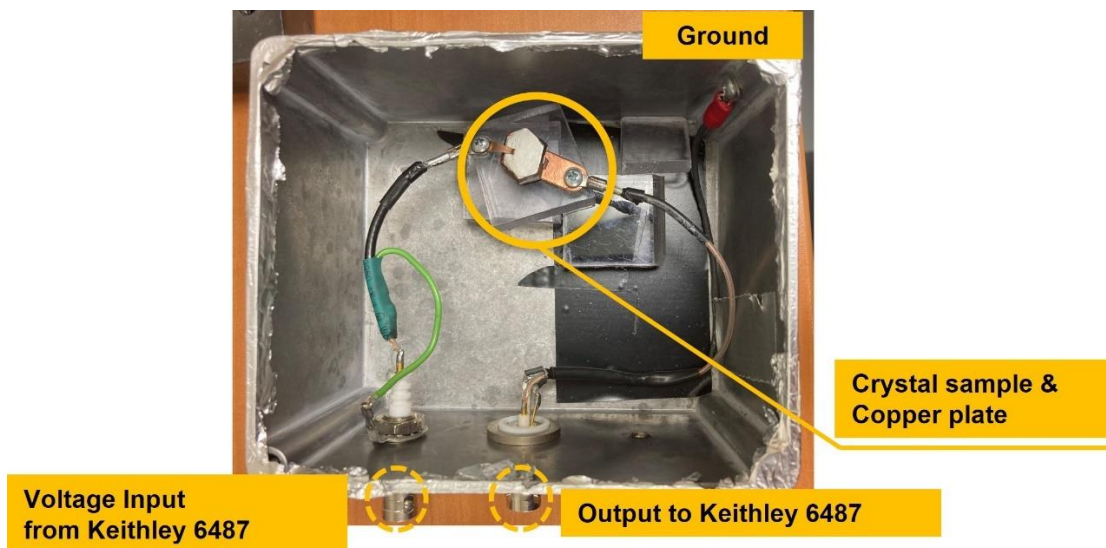


Figure 3.8 Home-made test box and fabricated detector device with copper plate.

As shown in Figure 3.9, the dark current and bias voltage represented the linearity relationship in the bias voltage range from -100 V to 100 V for pristine, 80°C-, and 120°C-annealed crystals, except 160°C-annealed crystal. The 160°C-annealed sample lost its current linearity to the corresponding bias voltage, which can be resulted from the thermal damage during temperature annealing process. The resistivity of pristine, 80°C-, and 120°C-annealed samples are displayed in 10^{10} magnitude order, which is high enough to get rid of the signal noises from the room temperature and environment, while the resistivity tend to decrease as annealing temperature increase. The resistivity of 120°C-annealed sample was $5.07 \times 10^{10} \Omega \text{ cm}$, which was about half value of the pristine sample's resistivity. This phenomenon of decreasing resistivity with increasing annealing temperature should be attributed to the fact that the temperature annealing improves the surface condition of $\text{FA}_3\text{Bi}_2\text{I}_9$ single crystal and stabilizes the disordered arrangement in the internal structure of the single crystal.

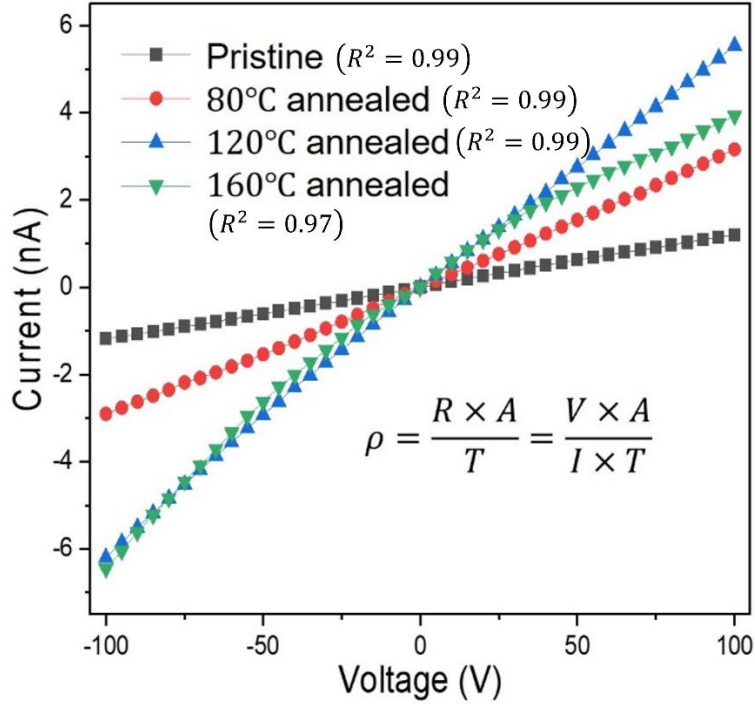


Figure 3.9 Dark currents versus corresponding bias voltage from -100 V to 100 V, investigated using pristine, 80°C-, 120°C-, and 160°C- annealed $\text{FA}_3\text{Bi}_2\text{I}_9$ single crystals at room temperature.

3.3.2 Space-Charge-Limited Current (SCLC)

In the space-charge-limited current (SCLC) curve, which is described in Figure 3.10, there are three regimes for explaining the electrical properties of $\text{FA}_3\text{Bi}_2\text{I}_9$ single crystal. The first region is Ohmic region, where the dark current is linearly proportional to the bias voltage. This region is usually used for estimating the resistivity of single crystals, due to the linear relationship between current and applied voltage. The second region is represented as trap-filled limit (TFL), which can be utilized to calculate the trap density of single crystal as following equation:

$$n_{\text{trap}} = \frac{2\varepsilon\varepsilon_0}{eL^2} V_{\text{TFL}}$$

where n_{trap} is the trap density, L is the thickness of the sample, V_{TFL} is the TFL voltage, ε is relative dielectric constant, and ε_0 vacuum dielectric constant. The trap-filled limit voltage, which can be determined at the point of intersection between ohmic and TFL. The third region, which

can be called the child region of SCLC curve, will start right after the TFL region and can be used to estimate the charge carriers' mobility.

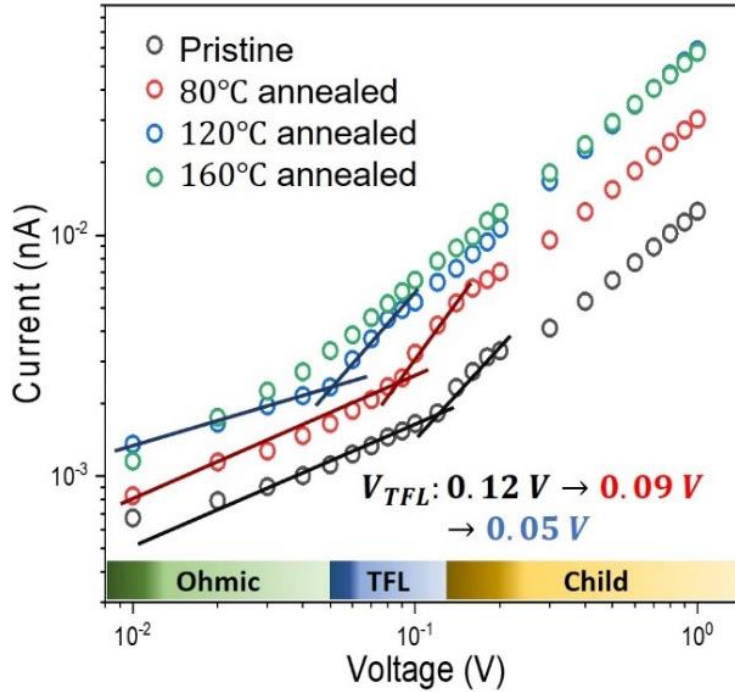


Figure 3.10 SCLC curve and each regions' transition point information using pristine, 80°C-, 120°C-, and 160°C-annealed FA₃Bi₂I₉ single crystals.

It is clear to find transition point of each region, which can be estimated by the change of the SCLC curves' slope, in case of pristine, 80°C-, and 120°C-annealed samples, while the transition points are hardly to be recognized for 160°C-annealed sample. The estimated TFL voltage of three types of FA₃Bi₂I₉ single crystals were 0.12 V, 0.09 V, and 0.05 V for pristine, 80°C-, and 120°C-annealed crystals, respectively. The calculated trap density (n_{trap}) of 120°C-annealed single crystal was $6.69 \times 10^8 \text{ cm}^{-3}$, which is much lower than the recent studies for another attracting perovskite for radiation detection, such as Cs₃Bi₂I₉ [70] and (BA)₂CsAgBiBr₇ [77].

CHAPTER 4: X-RAY RESPONSE PERFORMANCE

In this chapter, the X-ray and gamma-ray detection performances of $\text{FA}_3\text{Bi}_2\text{I}_9$ single crystals were described and the effect and influence of temperature annealing were verified as comparing the results of samples, which were applied by each temperature conditions. Mobility-lifetime ($\mu\tau$) product, sensitivity, signal-to-noise ratio (SNR), and detection limit from incident X-ray and photocurrent change from incident gamma-ray are described and elaborated.

4.1 X-ray On/Off test

X-ray response properties of $\text{FA}_3\text{Bi}_2\text{I}_9$ single crystal were investigated using Mini-X2 X-ray tube and controller, which uses Tungsten (W) for the target material and has the voltage range of 35-70 kV and current range of 5-200 μA . This X-ray tube can generate the dose rate from 0.61 to 17.25 $\mu\text{Gy/s}$ for the test. X-ray response test was conducted using $\text{Ag}/\text{FA}_3\text{Bi}_2\text{I}_9/\text{Ag}$ planar detector device with the incident X-ray generated from the top of the detector device, as described in Figure 4.2. The incident X-ray goes through the planar detector, which are followed by interaction between the medium material and the incident X-ray. This phenomenon induces the generation of charge carriers, i.e., electrons and holes, which creates the photocurrent.

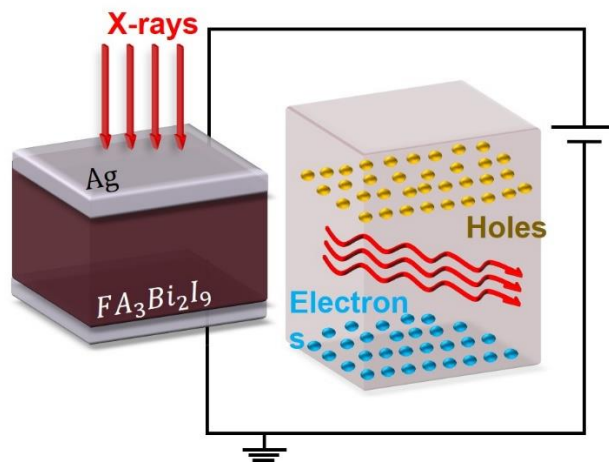


Figure 4.1 Schematic concept of X-ray response tests using $\text{Ag}/\text{FA}_3\text{Bi}_2\text{I}_9/\text{Ag}$ planar detector device.

Using the 120°C-annealed single crystal, which demonstrated the best optical and electrical quality among all samples, the photocurrents from incident X-ray are linearly proportional to the applied dose rate from 5.5 to 8.6 $\mu\text{Gy/s}$ at bias voltage of 40 V, as shown in Figure 4.3. It represents that FA3Bi2I9 single crystal can be effectively used for discriminating the different X-ray dose rates.

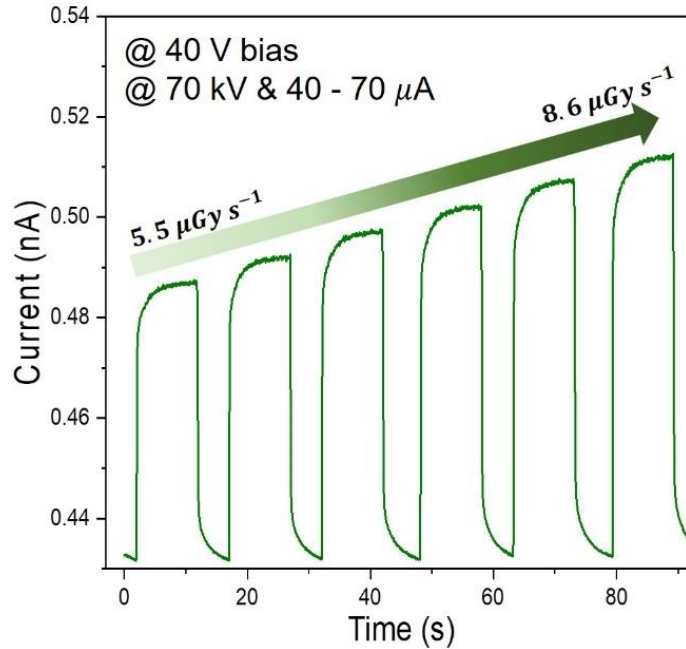


Figure 4.2 X-ray induced photocurrent of Ag/FA₃Bi₂I₉ (120°C-annealed)/Ag device under 40 V bias voltage.

The relationship of signal current-applied bias voltage is described in Figure 4.4. Comparing all samples' linearity of photocurrent from the different X-ray dose rate, except 160°C-annealed sample, all other samples showed clear photocurrent linearity to the different X-ray dose rate from 5.5 to 8.6 $\mu\text{Gy/s}$. In case of 160°C-annealed sample, there is an ambiguous region between X-ray dose rate of 7.0 to 7.5 $\mu\text{Gy/s}$ where photocurrent linearity is not established. It could come from the decomposition of the FA₃Bi₂I₉ single crystal structure and the degradation of perovskite layer caused by the high annealing temperature. It indicates that the quality and the performance of FA3Bi2I9 single crystal can be reduced at the annealing temperature above 160°C. The response

time of the interaction between the X-ray and detector material is one of the key factors in determining the quality of X-ray detector materials.

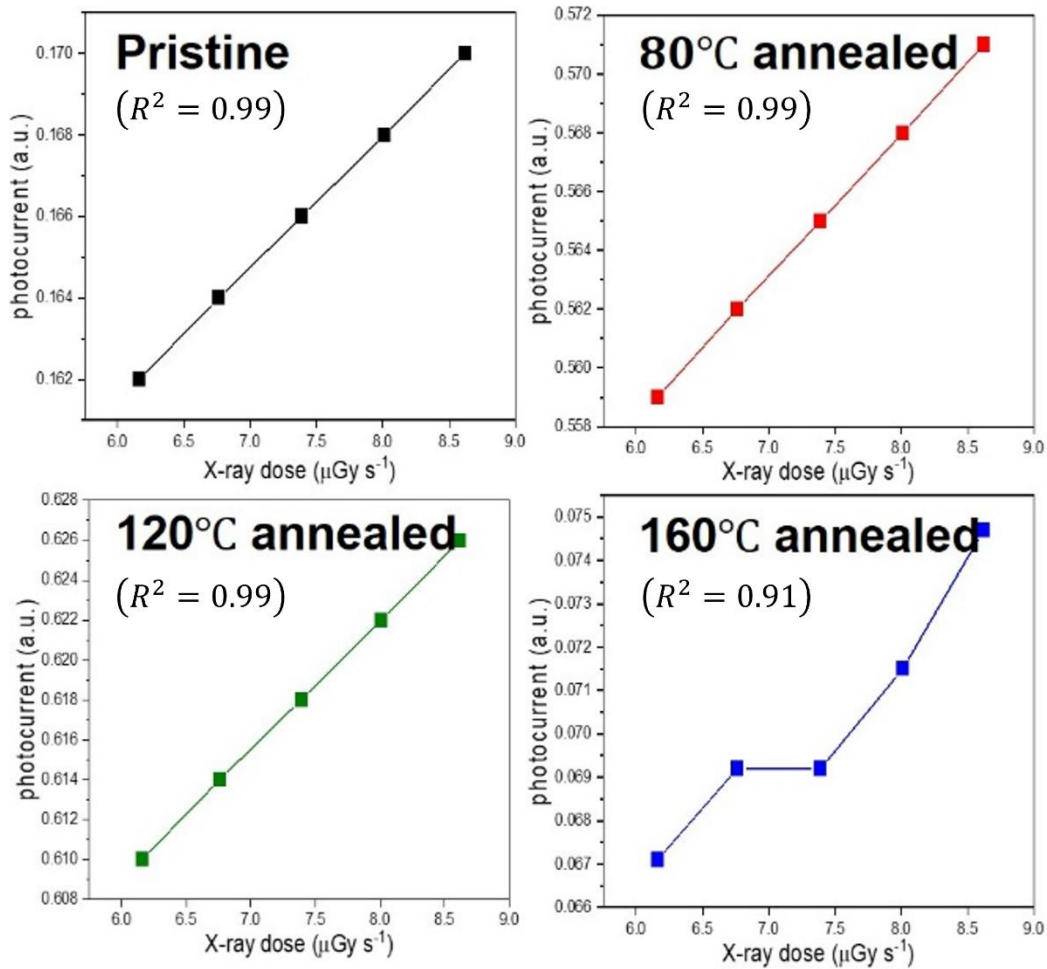


Figure 4.3 X-ray-dependent photocurrent of pristine, 80°C-, 120°C-, and 160°C-annealed $\text{FA}_3\text{Bi}_2\text{I}_9$ single crystal.

In Figure 4.5, the photocurrent rise times of pristine sample and 120°C-annealed sample were compared under X-ray dose rate of $17.25 \mu\text{Gy/s}$ with 10 V bias voltage. The rise time of 120°C-annealed crystal was 2.79, which was about 2 times faster than the pristine sample. Mobility (μ)-lifetime (τ) product, which means how the generated charge carriers can move fast and live long time, is another criterion to evaluate the performance of radiation detectors.

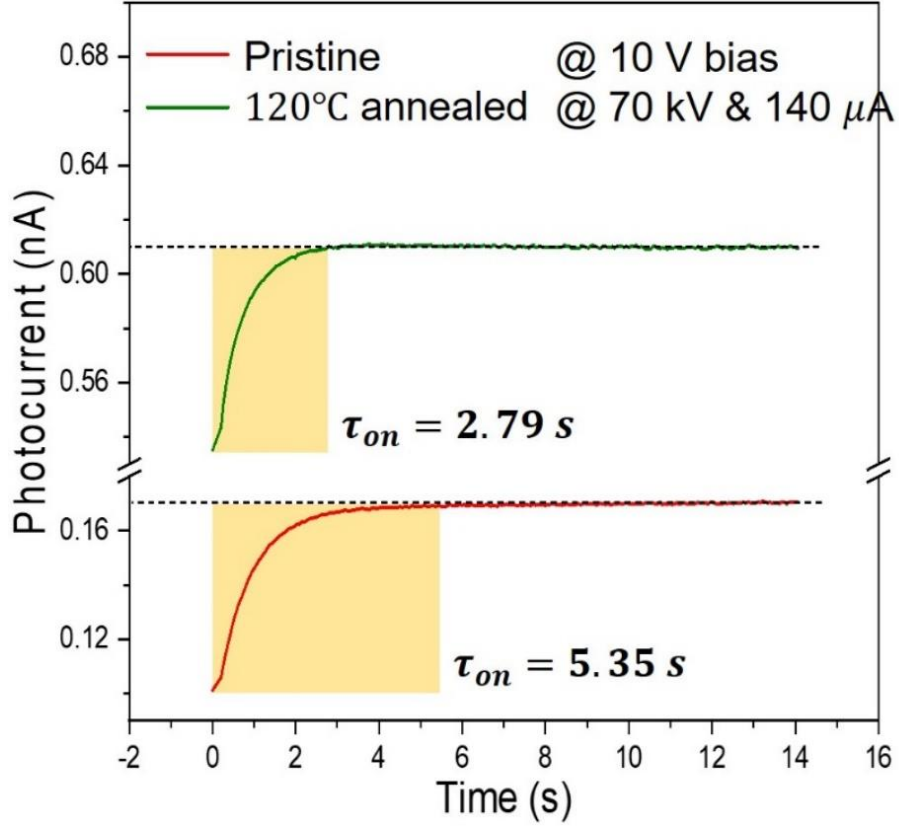


Figure 4.4 Rise time of pristine and 120°C-annealed FA₃Bi₂I₉ single crystal under 10 V bias.

4.2 Mobility-Lifetime ($\mu\tau$) Product and Sensitivity

As illustrated in Figure 4.6, signal current, which is the difference between photocurrent and dark current, corresponding to the applied bias voltage is indicated using 120°C-annealed crystal with X-ray dose rate of 7.39 $\mu\text{Gy/s}$. The saturated signal current was generated at 300 V bias voltage, which means that the charge collection efficiency (CCE) is optimized at 300 V bias voltage. The $\mu\tau$ product of the crystal can be derived using this information and modified Hecht equation [1][31]:

$$CCE \approx \frac{\mu\tau V}{d^2} \left(1 - e^{-\frac{d^2}{\mu\tau V}} \right)$$

where V is the applied corresponding bias voltage and d is the distance between the X-ray sources and the detector. The estimated $\mu\tau$ product of 120°C-annealed FA₃Bi₂I₉ single crystal is

$3.39 \times 10^{-4} \text{ cm}^2 \text{ V}^{-1}$, which is higher by two order of magnitude than the α -Se commercial radiation detector material [105] and guarantees that $\text{FA}_3\text{Bi}_2\text{I}_9$ single crystal can be a promising candidate for the effective X-ray detector.

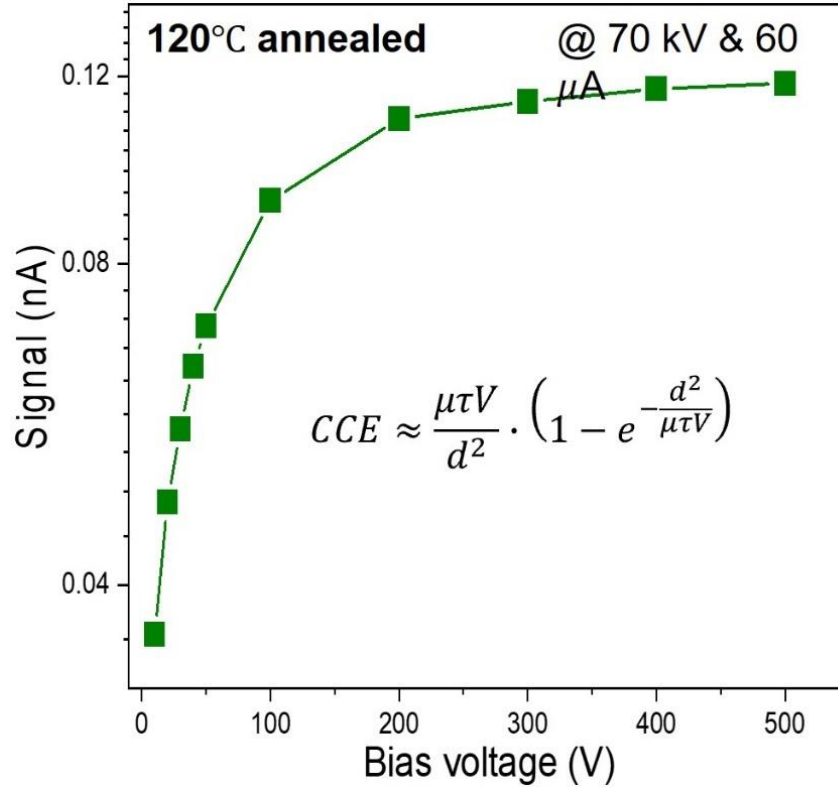


Figure 4.5 $\mu\tau$ product parameters extracted from the modified Hecht equation using CCE.

As described in Figure 4.7, the sensitivity of 120°C-annealed sample was acquired from the photocurrent caused by the X-ray dose rate of $5.54 \mu\text{Gy/s}$ under 40 V bias voltage. The sensitivity can be determined by the following equation [106]:

$$S = \frac{I_{ph}}{DA}$$

where I_{ph} is X-ray photocurrent, D is X-ray dose rate, and A is the detection area, i.e., surface area, of $\text{FA}_3\text{Bi}_2\text{I}_9$ single crystal sample. The calculated sensitivity was $804 \mu\text{C Gy}_{air}^{-1} \text{ cm}^{-2}$, which is higher than the previous work regarding the $\text{FA}_3\text{Bi}_2\text{I}_9$ single crystal.

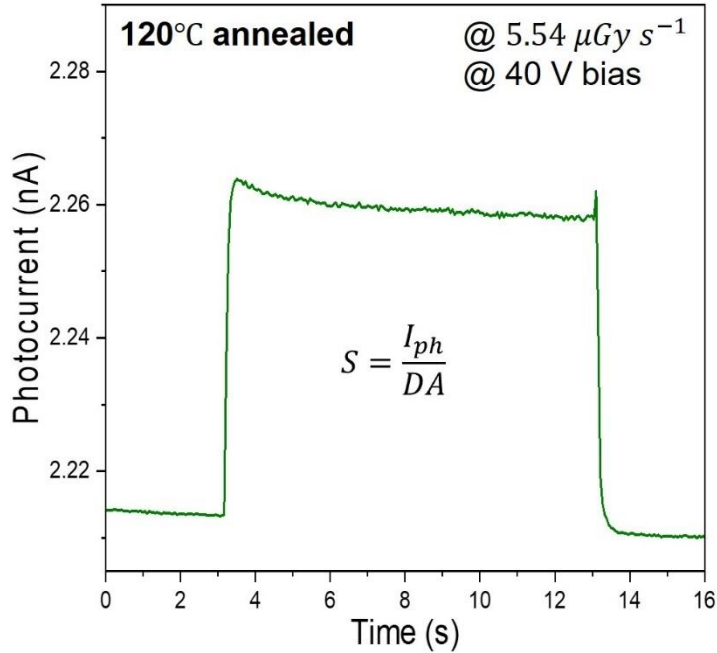


Figure 4.6 Sensitivity of 120°C-annealed FA₃Bi₂I₉ single crystal at X-ray dose rate of 5.54 μGy/s under 40 V bias voltage.

Taking a comprehensive look at the $\mu\tau$ product and the sensitivity for all samples, as depicted in Figure 4.8, both $\mu\tau$ product and the sensitivity results increase as annealing temperatures rise until 120°C, while 160°C-annealed sample's $\mu\tau$ product and the sensitivity rapidly decrease lower than the pristine sample's results. According to these consequences, the annealing temperature of 120°C is optimized to detect the X-ray radiation for FA₃Bi₂I₉ single crystal due to the highest charge carriers' transportation and sensitivity. However, it is apparent that the temperature of 160°C can cause significant damage, rendering FA₃Bi₂I₉ single crystal unable to perform as intended.

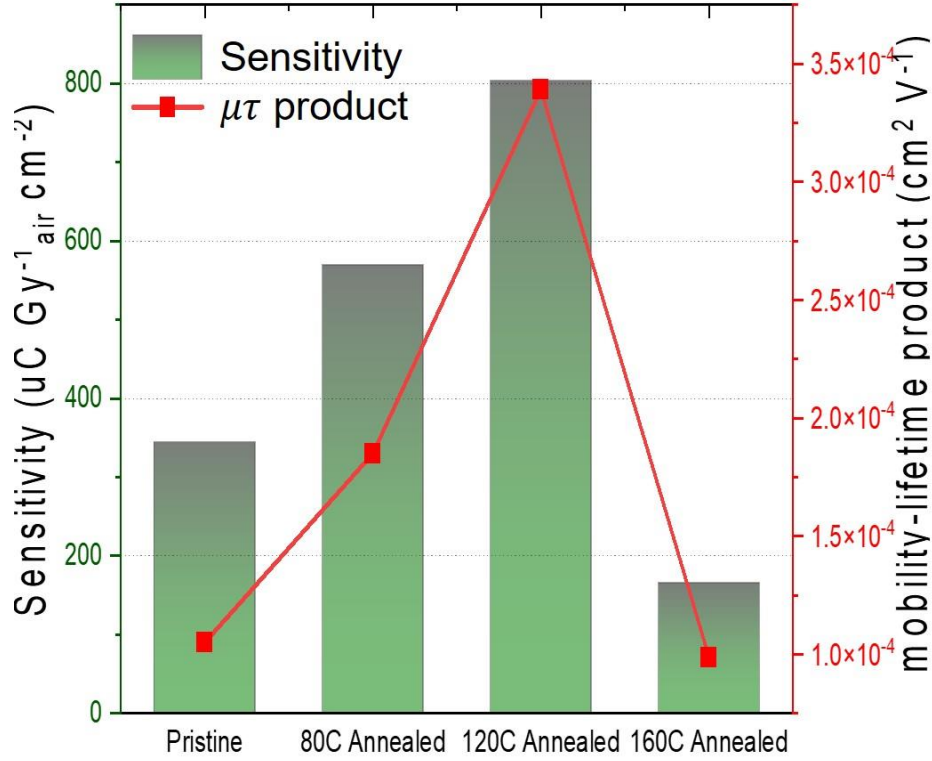


Figure 4.7 Comparison of $\mu\tau$ product and sensitivity from pristine, 80°C-, 120°C-, and 160°C-annealed FA₃Bi₂I₉ single crystal.

4.3 Signal-to-Noise Ratio (SNR) and Detection Limit

Signal-to-noise ratio (SNR) can be used to understand the properties of detector material and to optimize the fabrication condition according to the application purpose. SNR can be derived from the following equation [109]:

$$\frac{I_{signal} = I_{ph} - I_d}{I_{noise} = \sqrt{\frac{1}{N} \sum_{i=1}^N (I_i - \bar{I}_{ph})^2}} \quad (5)$$

where I_d is dark current and I_{noise} is noise current, which is derived by the standard deviation of the measured photocurrent. The SNR of three kinds of samples (pristine, 80°C-, and 120°C-annealed FA₃Bi₂I₉ single crystals) are displayed in Figure 4.9. Pristine and 80°C-annealed samples keep their SNR at high level until bias voltage of 100 V, followed by SNR decrease after 200 V

bias voltage. Simultaneously, the SNR of 120°C-annealed crystal increase until the bias voltage reaches 200 V. According to these SNR information, 120°C-annealed sample has a wide range of bias voltage, which can support the excellent X-ray detection ability compared with other annealing temperature applied samples.

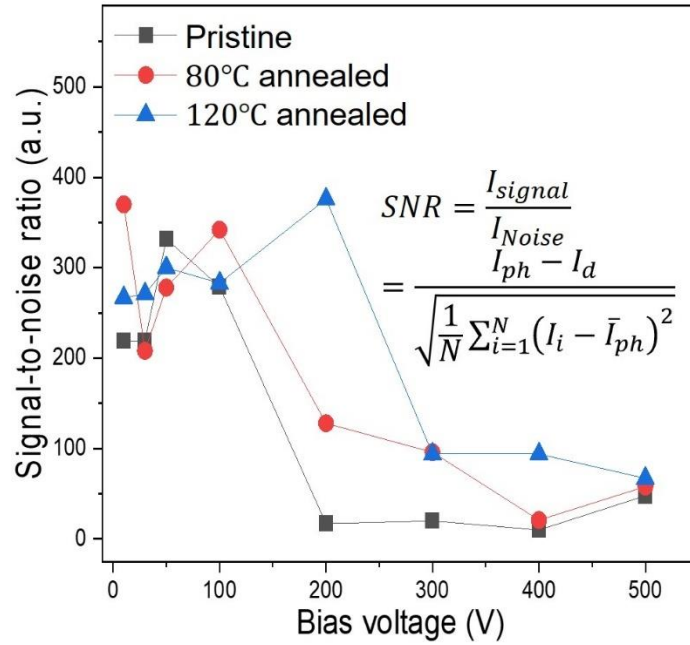


Figure 4.8 Comparison of X-ray dose rate-dependent SNR from pristine, 80°C-, and 120°C-annealed FA₃Bi₂I₉ single crystal.

Using the SNR data, the detection limit of 120°C-annealed FA₃Bi₂I₉ single crystal can be estimated, as described in Figure 4.10. The SNRs corresponding to X-ray dose rate are indicated in the graph with the y-axis (SNR value) in log-scale. Based on the description from the International Union of Pure and Applied Chemistry, the limit of detection is equivalent to an X-ray dose rate that provides an SNR value larger than three [106]. By using the linear interpolation method in the X-ray dose rate-dependent SNR data, the detection limit of 120°C-annealed FA₃Bi₂I₉ single crystal was 4.0 nGy s⁻¹, which is considerably outstanding value in X-ray detector material research.

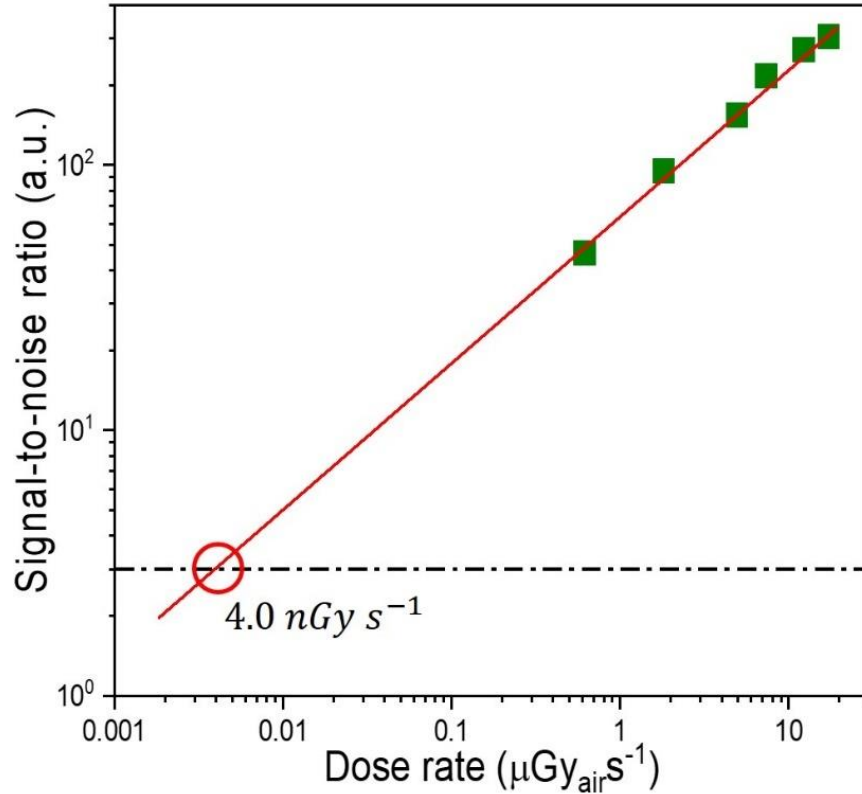


Figure 4.9 Detection limit of 120°C-annealed FA₃Bi₂I₉ single crystal using SNR data.

4.4 Stability

Stability issue is one of the main problems for hybrid perovskites to be used in various environmental applications. To evaluate if as-grown FA₃Bi₂I₉ single crystals have a good quality of stability to be used for extreme environmental applications, the most promising detector device, i.e., 120°C-annealed FA₃Bi₂I₉ single crystal-based planar detector device, was utilized for the measurement. X-ray was set up as 7.392 $\mu\text{Gy}/\text{s}$ with 70 kV and 60 μA configuration, while the bias voltage of 30 V entered the detector device. As shown in Figure 4.11, the dark and photocurrent under X-ray is maintained for 90 days from the first fabrication. There are some changes in exact dark current and photocurrent value, however, this variation is minor differences, which means that the quality and functionality of the as-grown FA₃Bi₂I₉ single crystal does not

change during about 90 days. This fact highly guarantees the $\text{FA}_3\text{Bi}_2\text{I}_9$ single crystal can be the promising candidate for commercial radiation detector materials.

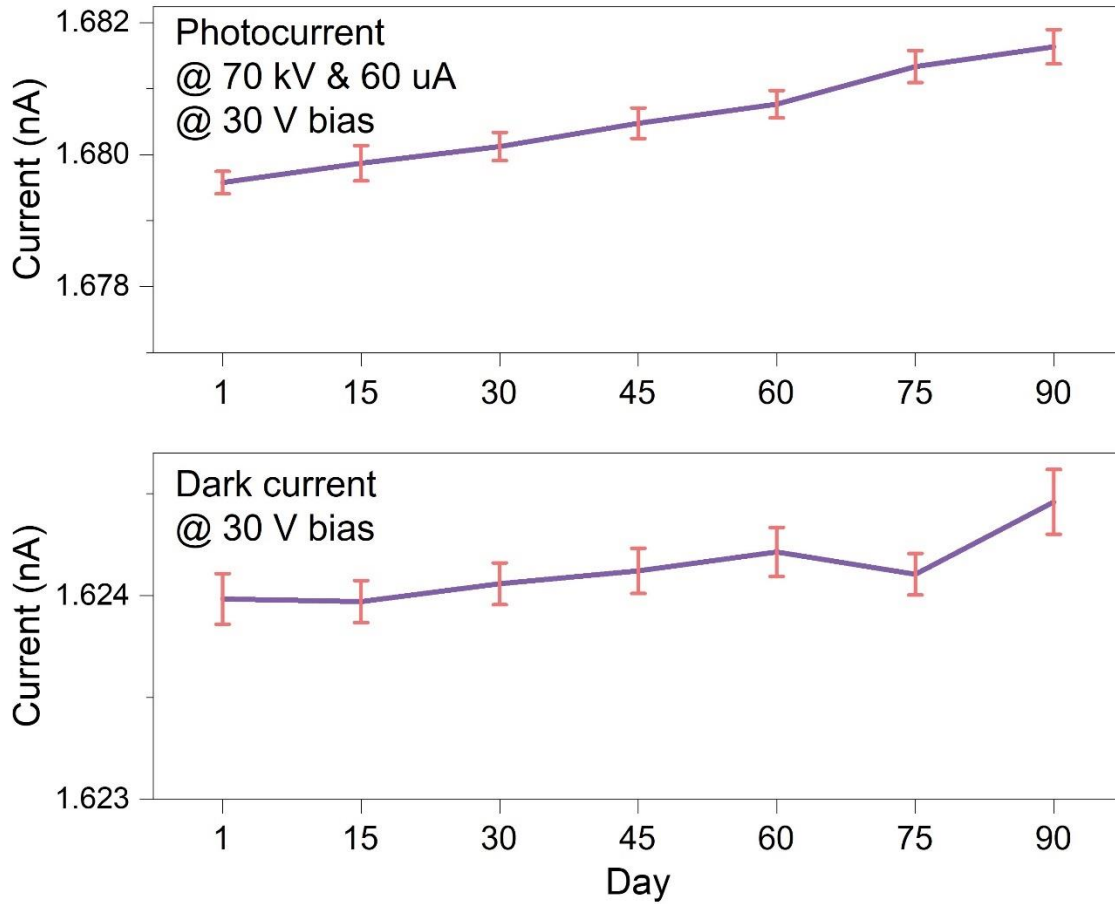


Figure 4.10 Photocurrent and dark current measurement of detector device fabricated using 120°C -annealed $\text{FA}_3\text{Bi}_2\text{I}_9$ single crystal every 15 days after first fabrication.

4.5 X-ray Imaging

X-ray imaging has been considered as an emerging research field due to its high possibility of being used for many applications, especially medical diagnostic systems. The principle of X-ray imaging by using semiconductors is almost the same as X-ray detectors, which were discussed in Chapter 1. Therefore, in the X-ray imaging field, hybrid perovskite single crystals can be an

outstanding candidate because of their high absorption coefficients, tunable bandgap, high detection efficiency, low detection limit, and especially cost-effective of fabrication.

We developed a customized testing setup for X-ray detection and obtained some X-ray imaging results, as described in Figure 4.11. The lead collimator with a hole whose size is 8mm or 1.2mm was prepared to control the resolution of the image from incident X-ray. For the 8mm resolution imaging, the word 'IC' fabricated by steel material was scanned at 36 rectangular shaped positions under X-ray dose rate of $6.16 \mu\text{Gy/s}$. The detector device was selected as Ag/FA₃Bi₂I₉ (pristine)/Ag and the bias voltage was 10 V, so that the word 'IC' was successfully imaged enough to be recognizable. Using the detector device Ag/FA₃Bi₂I₉ (120°C-annealed)/Ag, which demonstrated the highest performance in the electrical and X-ray response experiment, 1.2mm resolution X-ray imaging test was conducted with X-ray dose rate of $0.616 \mu\text{Gy/s}$, which is the lowest X-ray dose rate using Mini-2 X-ray tube. We imagined a key with a steel core wrapped in a composite material of rubber and plastic at the handle and were able to obtain the expected shape through X-ray imaging at 1300 points. However, the lack of precision in imaging the curved portion was noted as an issue, which can be overcome by improving experimental factors for scanning with a resolution of less than 1mm. Also, in the handle part, it was difficult to distinguish the photocurrent between the portion made only of the composite material and the part where the steel and the composite material overlap. This issue is expected to be overcome by applying more advanced single crystal growth methods or detector fabrication methods.

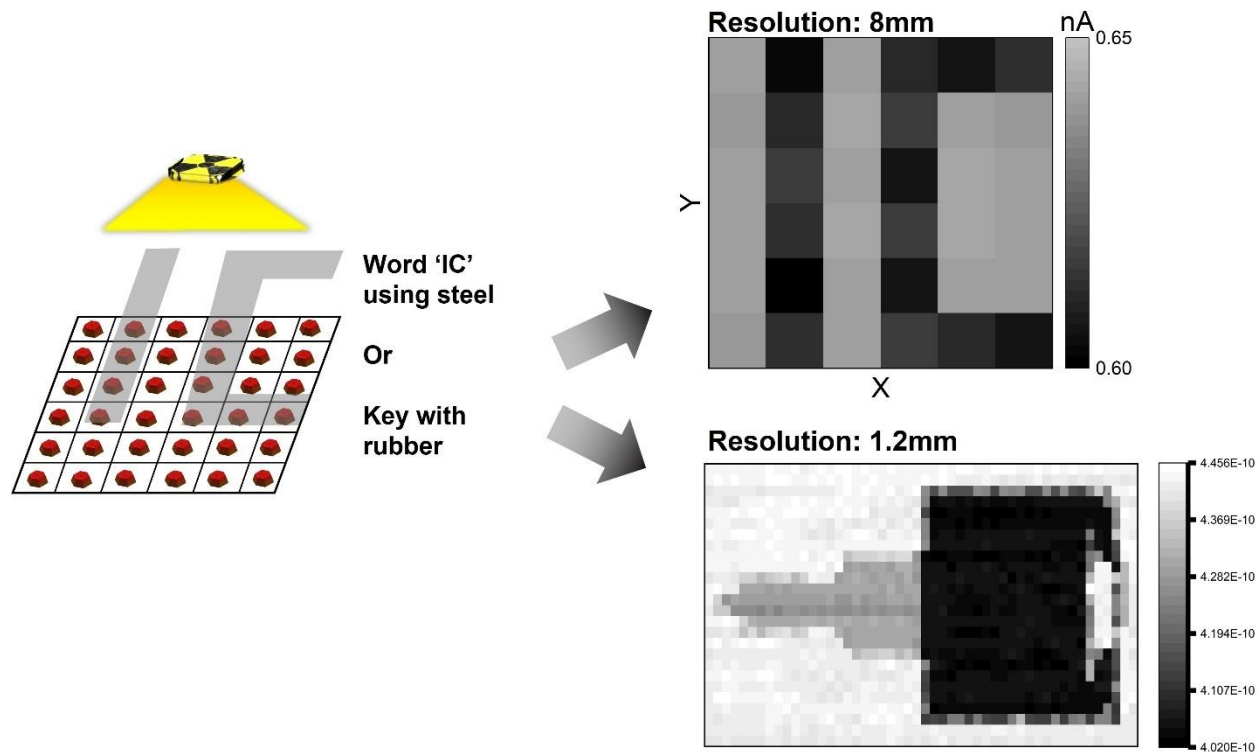


Figure 4.11 X-ray imaging results using Ag/FA₃Bi₂I₉ (pristine and 120°C-annealed)/Ag planar detector device from 8mm and 1.2mm lead collimator attached configuration.

CHAPTER 5: CONCLUSION AND FUTURE WORK

This chapter provide the summary and conclusion of this work for the development of lead-free hybrid perovskite FA₃Bi₂I₉ single crystal, which are followed by the expected future work to enhance the radiation detection performance and to guarantee the commercialization.

5.1 Summary and Conclusion

In this work, we successfully grew the temperature-annealed lead-free bismuth-based FA₃Bi₂I₉ single crystal by seeded solution-based evaporation method and prepared Ag/FA₃Bi₂I₉/Ag planar detector device. The seeded method can offer an opportunity to obtain the bulk FA₃Bi₂I₉ single crystals with reasonable production cost and their quality is guaranteed by XRD and UV-vis measurement. The investigated results demonstrate that the 120°C annealing temperatures provided the most improved quality of FA₃Bi₂I₉ single crystal, while the 160°C annealing temperatures can reduce the performance of the single crystal and generate substantial damage to the structure of FA₃Bi₂I₉ single crystal, which can influence the optical, electrical, and X-ray response properties. The temperature-annealed FA₃Bi₂I₉ single crystal can be a promising candidate for X-ray detector materials, due to its high resistivity of $5.06 \times 10^{10} \Omega \text{ cm}$ with wide bandgap of 1.97 eV, high enough $\mu\tau$ product of $3.39 \times 10^{-4} \text{ cm}^2 \text{ V}^{-1}$, and superb sensitivity of $804 \mu\text{C Gy}_{\text{air}}^{-1} \text{ cm}^{-2}$ with extremely low detection limit of 4.0 nGy s^{-1} . Given these advantages, temperature-annealed FA₃Bi₂I₉ single crystal has significant potential for application in various fields as a future X-ray detector material. At the same time, further research is encouraged to improve the temperature annealing condition and device fabrication method to optimize the accomplishment of FA₃Bi₂I₉ single crystal.

Table 5.1 The comprehensive radiation detection performances of pristine, 80°C, 120°C, and 160°C-annealed FA₃Bi₂I₉ single crystal in this work.

	Pristine	80°C-annealed	120°C-annealed	160°C-annealed
Bandgap (eV)	1.97	1.97	1.97	1.97
Resistivity ($\Omega\text{ cm}$)	9.27×10^{10}	5.90×10^{10}	5.07×10^{10}	8.56×10^{10}
Trap density (cm^{-3})	1.61×10^9	1.20×10^9	6.69×10^8	-
$\mu\tau$ product ($\text{cm}^2\text{ V}^{-1}$)	0.000105	0.000185	0.000339	0.000099
Sensitivity ($\mu\text{C Gy}_{\text{air}}^{-1}\text{ cm}^{-2}$)	345	570	804	166
Detection limit (nGy s^{-1})	40	10	4.0	1000

Comparing the X-ray detection performance of 120°C-annealed FA₃Bi₂I₉ single crystal with recent investigated lead-free bismuth-based perovskite single crystal (Table 5.2), it is clear that the FA₃Bi₂I₉ single crystal can be a promising candidate for the radiation detector. The trap density of 120°C-annealed FA₃Bi₂I₉ single crystal is extremely lower than the others with the order of 10^8 cm^{-3} . For the $\mu\tau$ product, there are other type of perovskites with higher value, however, there is a progress compared with the FA₃Bi₂I₉ single crystal investigated in 2021 [40]. The sensitivity is also relatively high except the Cs₃Bi₂I₉ single crystal explored in 2022 [108]. The detection limit of 120°C-annealed FA₃Bi₂I₉ single crystal is extremely low, which is about 50 times lower than the previous work of FA₃Bi₂I₉ single crystal [40] and Cs₂AgBiBr₆ single crystal [107]. Therefore, we can tell the FA₃Bi₂I₉ single crystal coupled with post-growth temperature annealing strategy have strong potential for the radiation detector material.

Table 5.2 The comparison of X-ray detection performance among the lead-free bismuth-based perovskite single crystal materials

	Trap density (cm^{-3})	$\mu\tau$ product ($cm^2 V^{-1}$)	Sensitivity ($\mu C Gy_{air}^{-1} cm^{-2}$)	Detection limit ($nGy s^{-1}$)
FA ₃ Bi ₂ I ₉ with 120°C annealing (This work)	6.69×10⁸	0.000339	804 under 50 V	4.0
Cs ₂ AgBiBr ₆ ([107]/2022)	1.18×10 ⁹	0.000536	325.78 under 4V	241
Cs ₃ Bi ₂ I ₉ ([108]/2022)	2.56×10 ⁹	0.00135	4382 under 20 V	7.93
FA ₃ Bi ₂ I ₉ (/2021)	9.48×10 ⁹	0.00013	598.1 under 500 V	200
MA ₃ Bi ₂ I ₉ (/2020)	-	-	872 under 100 V	31
AgBi ₂ I ₇ (/2020)	3.78×10 ¹⁰	0.0034	282.5 under 500 V	72

Note: The '-' symbol in the table indicates that the results are not provided in the reference

5.2 Future work

According to the experimental results from temperature-annealed FA₃Bi₂I₉ single crystal-based detector device, this kind of hybrid bismuth-based perovskite single crystal has a highly promising potential to be used for radiation detector materials, due to wide bandgap, high resistivity, low trap density, and excellent performance in $\mu\tau$ product, sensitivity, and limit of detection under X-ray. However, there are some challenges to be overcome, which would be the future work regarding FA₃Bi₂I₉ single crystal for radiation detection following by this work.

First, the verification of detection ability under incident high energy radiation and charged particles, i.e., alpha particle, should be conducted. There are several kinds of research regarding gamma-ray detection performance using hybrid perovskite materials, such as Cs₂AgBiBr₆ [97],

MAPbBr_xCl_{3-x} [110], and CsPbBr₃ [111]. However, there is a lack of related research using formamidinium (FA)-based perovskite and lead-free perovskites for radiation detection. High energy gamma-ray can penetrate the detection medium material easily. As such acquiring thick detector medium is crucial to effectively detect gamma-ray. It is possible to grow the bulk size of single crystal using seeded-evaporation method, as described in Chapter 2. Thus, obtaining the spectra from gamma-ray and alpha particle sources, such as Cs¹³⁷, Co⁶⁰, and Am²⁴¹ would be the next step for further exploring FA₃Bi₂I₉ single crystals for the detection of high energy radiation.

Second, high resolution X-ray imaging should be explored as the next step to obtain high quality X-ray imaging. Using the collimator of μm unit size and resolution stage, which can be operated automatically with slow moving step and speed, the high-resolution X-ray image can be collected. Fabrication of pixelated detector device can provides another promising option for high resolution X-ray imaging [112].

Third, the diversification of device fabrication methods should be considered to improve the radiation detection performance of the hybrid perovskite single crystals. Perovskite single crystals' ion migration and stability issues have not been fully addressed. Ion migration affects the quality of radiation detection efficiency, and it can change the structure of the perovskite single crystals over time. Especially for hybrid perovskite single crystals, due to its intrinsic structure, there is a possibility to lose its operation stability in extreme environment over long operation time. Fabrication using guard ring, passivation, and doping could provide a potential solution to enhance the detector performance.

REFERENCES

- [1] Kim, D., & Yang, G. (2022). Perovskite materials: from single crystals to radiation detection. *CrystEngComm*, 24(30), 5383-5399.
- [2] Klann, R. T., Shergur, J., & Mattesich, G. (2009). Current state of commercial radiation detection equipment for homeland security applications. *Nuclear technology*, 168(1), 79-88.
- [3] Pashby, J., Glenn, S., Divin, C., & Martz, H. (2017). *Radiation Detection and Dual-Energy X-Ray Imaging for Port Security* (No. LLNL-TR--736549). Lawrence Livermore National Lab.(LLNL).
- [4] Deyglun, C., Weber, A., Pepin, N., Funk, P., & Lambert, T. (2018). *Testing and performances of radiation detection instruments for nuclear security* (No. IAEA-CN--269).
- [5] Lu, L., Sun, M., Lu, Q., Wu, T., & Huang, B. (2021). High energy X-ray radiation sensitive scintillating materials for medical imaging, cancer diagnosis and therapy. *Nano Energy*, 79, 105437.
- [6] Gill, H. S., Elshahat, B., Kokil, A., Li, L., Mosurkal, R., Zygmanski, P., ... & Kumar, J. (2018). Flexible perovskite based X-ray detectors for dose monitoring in medical imaging applications. *Physics in Medicine*, 5, 20-23.
- [7] Lu, Y., & Lu, R. (2017). Non-destructive defect detection of apples by spectroscopic and imaging technologies: a review. *Transactions of the ASABE*, 60(5), 1765-1790.
- [8] Hubbell, J. H. (2006). Electron–positron pair production by photons: A historical overview. *Radiation Physics and Chemistry*, 75(6), 614-623.
- [9] Choppin, G., Liljenzin, J. O., & Rydberg, J. (2002). *Radiochemistry and nuclear chemistry*. Butterworth-Heinemann.

- [10] Sakai, H., Yoshii, T., Takasaki, F., & Kawarabayashi, J. (2021). Evaluation of the detection limit of net count in peak for the energy spectrum of CZT detector. *Applied Radiation and Isotopes*, 169, 109569.
- [11] Chen, H., Li, H., Reed, M. D., Sundaram, A. G., Eger, J., Hugg, J. W., ... & He, Z. (2018, September). Development of large-volume high-performance monolithic CZT radiation detector. In *Hard X-Ray, Gamma-Ray, and Neutron Detector Physics XX*(Vol. 10762, p. 107620N). International Society for Optics and Photonics.
- [12] Pennicard, D., Pirard, B., Tolbanov, O., & Iniewski, K. (2017). Semiconductor materials for x-ray detectors. *MRS Bulletin*, 42(6), 445-450.
- [13] Basiricò, L., Ciavatti, A., & Fraboni, B. (2021). Solution-Grown Organic and Perovskite X-Ray Detectors: A New Paradigm for the Direct Detection of Ionizing Radiation. *Advanced Materials Technologies*, 6(1), 2000475.
- [14] Akkerman, Q. A., & Manna, L. (2020). What defines a halide perovskite?. *ACS energy letters*, 5(2), 604-610.
- [15] Ni, Z., Bao, C., Liu, Y., Jiang, Q., Wu, W. Q., Chen, S., ... & Huang, J. (2020). Resolving spatial and energetic distributions of trap states in metal halide perovskite solar cells. *Science*, 367(6484), 1352-1358.
- [16] Brakkee, R., & Williams, R. M. (2020). Minimizing defect states in lead halide perovskite solar cell materials. *Applied Sciences*, 10(9), 3061.
- [17] Tian, J., Xue, Q., Yao, Q., Li, N., Brabec, C. J., & Yip, H. L. (2020). Inorganic halide perovskite solar cells: progress and challenges. *Advanced Energy Materials*, 10(23), 2000183.
- [18] Liu, S., Guan, Y., Sheng, Y., Hu, Y., Rong, Y., Mei, A., & Han, H. (2020). A review on additives for halide perovskite solar cells. *Advanced Energy Materials*, 10(13), 1902492.

- [19] Tsai, H., Liu, F., Shrestha, S., Fernando, K., Tretiak, S., Scott, B., ... & Nie, W. (2020). A sensitive and robust thin-film x-ray detector using 2D layered perovskite diodes. *Science advances*, 6(15), eaay0815.
- [20] Liu, D., Hu, Z., Hu, W., Wangyang, P., Yu, K., Wen, M., ... & Zang, Z. (2017). Two-step method for preparing all-inorganic CsPbBr₃ perovskite film and its photoelectric detection application. *Materials Letters*, 186, 243-246.
- [21] Basiricò, L., Senanayak, S. P., Ciavatti, A., Abdi-Jalebi, M., Fraboni, B., & Siringhaus, H. (2019). Detection of X-rays by solution-processed cesium-containing mixed triple cation perovskite thin films. *Advanced Functional Materials*, 29(34), 1902346.
- [22] Shrestha, S., Fischer, R., Matt, G. J., Feldner, P., Michel, T., Osvet, A., ... & Brabec, C. J. (2017). High-performance direct conversion X-ray detectors based on sintered hybrid lead triiodide perovskite wafers. *Nature Photonics*, 11(7), 436-440.
- [23] Daum, M., Deumel, S., Sytnyk, M., Afify, H. A., Hock, R., Eigen, A., ... & Heiss, W. (2021). Self-Healing Cs₃Bi₂Br₃I₆ Perovskite Wafers for X-Ray Detection. *Advanced Functional Materials*, 31(47), 2102713.
- [24] Han, M., Sun, J., Peng, M., Han, N., Chen, Z., Liu, D., ... & Yang, Z. X. (2019). Controllable growth of lead-free all-inorganic perovskite nanowire array with fast and stable near-infrared photodetection. *The Journal of Physical Chemistry C*, 123(28), 17566-17573.
- [25] Ye, F., Lin, H., Wu, H., Zhu, L., Huang, Z., Ouyang, D., ... & Choy, W. C. (2019). High-quality cuboid CH₃NH₃PbI₃ single crystals for high performance X-ray and photon detectors. *Advanced Functional Materials*, 29(6), 1806984.

- [26] Gou, Z., Liu, W., Huanglong, S., Zhu, X., Sun, H., Yang, D., & Wangyang, P. (2019). Self-Powered X-Ray Photodetector Based on Ultrathin PbI₂ Single Crystal. *IEEE Electron Device Letters*, 40(4), 578-581.
- [27] Gao, L., & Yan, Q. (2020). Recent advances in lead halide perovskites for radiation detectors. *Solar RRL*, 4(2), 1900210.
- [28] Zhang, Z., & Yang, G. (2021). Recent advancements in using perovskite single crystals for gamma-ray detection. *Journal of Materials Science: Materials in Electronics*, 32, 12758-12770.
- [29] Zhang, H., Xu, Y., Sun, Q., Dong, J., Lu, Y., Zhang, B., & Jie, W. (2018). Lead free halide perovskite Cs₃Bi₂I₉ bulk crystals grown by a low temperature solution method. *Cryst EngComm*, 20(34), 4935-4941.
- [30] Bhaumik, S., Ray, S., & Batabyal, S. K. (2020). Recent advances of lead-free metal halide perovskite single crystals and nanocrystals: synthesis, crystal structure, optical properties, and their diverse applications. *Materials Today Chemistry*, 18, 100363.
- [31] Wang, Y. X., Pan, Z. Y., Ho, Y. K., Xu, Y., & Du, A. J. (2001). Nuclear instruments and methods in physics research section B: beam interactions with materials and atoms. *Nuclear Instruments and Methods in Physics Research B*, 180(1-4), 251-256.
- [32] Wei, H., Fang, Y., Mulligan, P., Chuirazzi, W., Fang, H. H., Wang, C., ... & Huang, J. (2016). Sensitive X-ray detectors made of methylammonium lead tribromide perovskite single crystals. *Nature Photonics*, 10(5), 333-339.
- [33] Wei, H., & Huang, J. (2019). Halide lead perovskites for ionizing radiation detection. *Nature communications*, 10(1), 1-12.

- [34] Wu, H., Ge, Y., Niu, G., & Tang, J. (2021). Metal halide perovskites for X-ray detection and imaging. *Matter*, 4(1), 144-163.
- [35] Geng, X., Zhang, H., Ren, J., He, P., Zhang, P., Feng, Q., ... & Ren, T. L. (2021). High-performance single crystal CH₃NH₃PbI₃ perovskite x-ray detector. *Applied Physics Letters*, 118(6), 063506.
- [36] Kasap, S.O. (2000). X-ray sensitivity of photoconductors: application to stabilized a-Se. *J. Phys. D Appl. Phys.* 33, 2853.
- [37] Phillips, W. C., Stewart, A., Stanton, M., Naday, I., & Ingersoll, C. (2002). High-sensitivity CCD-based X-ray detector. *Journal of synchrotron radiation*, 9(1), 36-43.
- [38] Zhang, H., Wang, F., Lu, Y., Sun, Q., Xu, Y., Zhang, B. B., ... & Kanatzidis, M. G. (2020). High-sensitivity X-ray detectors based on solution-grown caesium lead bromide single crystals. *Journal of Materials Chemistry C*, 8(4), 1248-1256.
- [39] Pan, W., Wu, H., Luo, J., Deng, Z., Ge, C., Chen, C., ... & Tang, J. (2017). Cs₂AgBiBr₆ single-crystal X-ray detectors with a low detection limit. *Nature photonics*, 11(11), 726-732.
- [40] Li, W., Xin, D., Tie, S., Ren, J., Dong, S., Lei, L., ... & Zhang, W. H. (2021). Zero-Dimensional Lead-Free FA₃Bi₂I₉ Single Crystals for High-Performance X-ray Detection. *The Journal of Physical Chemistry Letters*, 12(7), 1778-1785.
- [41] Liu, H., Lee, J., & Kang, J. (2020). Characteristics of a hybrid detector combined with a perovskite active layer for indirect X-ray detection. *Sensors*, 20(23), 6872.
- [42] Dualeh, A., Tétreault, N., Moehl, T., Gao, P., Nazeeruddin, M. K., & Grätzel, M. (2014). Effect of annealing temperature on film morphology of organic–inorganic hybrid perovskite solid-state solar cells. *Advanced Functional Materials*, 24(21), 3250-3258.

- [43] Zhang, H., Dun, G., Feng, Q., Zhao, R., Liang, R., Gao, Z., ... & Ren, T. L. (2020). Encapsulated X-ray detector enabled by all-inorganic lead-free perovskite film with high sensitivity and low detection limit. *IEEE Transactions on Electron Devices*, 67(8), 3191-3198.
- [44] Demir, N., & Kuluöztürk, Z. N. (2021). Determination of energy resolution for a NaI (Tl) detector modeled with FLUKA code. *Nuclear Engineering and Technology*, 53(11), 3759-3763.
- [45] Moszyński, M., Zalipska, J., Balcerzyk, M., Kapusta, M., Mengesha, W., & Valentine, J. D. (2002). Intrinsic energy resolution of NaI (Tl). *Nuclear Instruments and Methods in Physics Research Section A: Accelerators, Spectrometers, Detectors and Associated Equipment*, 484(1-3), 259-269.
- [46] Szymańska, K., Achenbach, P., Agnello, M., Botta, E., Bracco, A., Bressani, T., ... & Wieland, O. (2008). Resolution, efficiency and stability of HPGe detector operating in a magnetic field at various gamma-ray energies. *Nuclear Instruments and Methods in Physics Research Section A: Accelerators, Spectrometers, Detectors and Associated Equipment*, 592(3), 486-492.
- [47] Zhang, H., Wang, F., Lu, Y., Sun, Q., Xu, Y., Zhang, B. B., ... & Kanatzidis, M. G. (2020). High-sensitivity X-ray detectors based on solution-grown caesium lead bromide single crystals. *Journal of Materials Chemistry C*, 8(4), 1248-1256.
- [48] Xu, Q., Wang, X., Zhang, H., Shao, W., Nie, J., Guo, Y., ... & Ouyang, X. (2020). CsPbBr₃ single crystal X-ray detector with Schottky barrier for X-ray imaging application. *ACS Applied Electronic Materials*, 2(4), 879-884.

- [49] Nazarenko, O., Yakunin, S., Morad, V., Cherniukh, I., & Kovalenko, M. V. (2017). Single crystals of caesium formamidinium lead halide perovskites: solution growth and gamma dosimetry. *NPG Asia Materials*, 9(4), e373-e373.
- [50] Cheng, Y., Sun, Q., Zhang, P., Wang, F., Zhang, B., Zhang, G., ... & Xu, Y. (2020). Secondary phase particles in cesium lead bromide perovskite crystals: An insight into the formation of matrix-controlled inclusion. *The Journal of Physical Chemistry Letters*, 11(14), 5625-5631.
- [51] Wei, W., Zhang, Y., Xu, Q., Wei, H., Fang, Y., Wang, Q., ... & Huang, J. (2017). Monolithic integration of hybrid perovskite single crystals with heterogenous substrate for highly sensitive X-ray imaging. *Nature Photonics*, 11(5), 315-321.
- [52] Wei, H., DeSantis, D., Wei, W., Deng, Y., Guo, D., Savenije, T. J., ... & Huang, J. (2017). Dopant compensation in alloyed $\text{CH}_3\text{NH}_3\text{PbBr}_{3-x}\text{Cl}_x$ perovskite single crystals for gamma-ray spectroscopy. *Nature materials*, 16(8), 826-833.
- [53] He, Y., Ke, W., Alexander, G. C., McCall, K. M., Chica, D. G., Liu, Z., ... & Kanatzidis, M. G. (2018). Resolving the energy of γ -ray photons with MAPbI_3 single crystals. *Acs Photonics*, 5(10), 4132-4138.
- [54] Wang, X., Wu, Y., Li, G., Wu, J., Zhang, X., Li, Q., ... & Lei, W. (2018). Ultrafast Ionizing Radiation Detection by p-n Junctions Made with Single Crystals of Solution-Processed Perovskite. *Advanced Electronic Materials*, 4(11), 1800237.
- [55] Huang, Y., Qiao, L., Jiang, Y., He, T., Long, R., Yang, F., ... & Chen, J. (2019). A-site Cation Engineering for Highly Efficient MAPbI_3 Single-Crystal X-ray Detector. *Angewandte Chemie International Edition*, 58(49), 17834-17842.

- [56] Ye, F., Lin, H., Wu, H., Zhu, L., Huang, Z., Ouyang, D., ... & Choy, W. C. (2019). High-quality cuboid $\text{CH}_3\text{NH}_3\text{PbI}_3$ single crystals for high performance X-ray and photon detectors. *Advanced Functional Materials*, 29(6), 1806984.
- [57] Fan, Z., Liu, J., Zuo, W., Liu, G., He, X., Luo, K., ... & Liao, C. (2020). Solution-Processed MAPbBr_3 and CsPbBr_3 Single-Crystal Detectors with Improved X-Ray Sensitivity via Interfacial Engineering. *physica status solidi (a)*, 217(9), 2000104.
- [58] Murgulov, V., Schweinle, C., Daub, M., Hillebrecht, H., Fiederle, M., Dědič, V., & Franc, J. (2021). Growth and Characterisation of Layered (BA) 2CsAgBiBr_7 Double Perovskite Single Crystals for Application in Radiation Sensing. *Crystals*, 11(10), 1208.
- [59] Lampert, M.A.; Mark, P. *Current Injections in Solids*; Electrical current series; Academic Press: Cambridge, MA, USA, 1970; p. 354.
- [60] Clinckemalie, L., Valli, D., Roeffaers, M. B., Hofkens, J., Pradhan, B., & Debroye, E. (2021). Challenges and Opportunities for CsPbBr_3 Perovskites in Low-and High-Energy Radiation Detection. *ACS Energy Letters*, 6(4), 1290-1314.
- [61] He, Y., Matei, L., Jung, H. J., McCall, K. M., Chen, M., Stoumpos, C. C., ... & Kanatzidis, M. G. (2018). High spectral resolution of gamma-rays at room temperature by perovskite CsPbBr_3 single crystals. *Nature communications*, 9(1), 1-8.
- [62] He, Y., Liu, Z., McCall, K. M., Lin, W., Chung, D. Y., Wessels, B. W., & Kanatzidis, M. G. (2019). Perovskite CsPbBr_3 single crystal detector for alpha-particle spectroscopy. *Nuclear Instruments and Methods in Physics Research Section A: Accelerators, Spectrometers, Detectors and Associated Equipment*, 922, 217-221.

- [63] Li, J., Du, X., Niu, G., Xie, H., Chen, Y., Yuan, Y., ... & Yang, B. (2019). Rubidium doping to enhance carrier transport in CsPbBr₃ single crystals for high-performance X-ray detection. *ACS applied materials & interfaces*, 12(1), 989-996.
- [64] He, Y., Petryk, M., Liu, Z., Chica, D. G., Hadar, I., Leak, C., ... & Kanatzidis, M. G. (2021). CsPbBr₃ perovskite detectors with 1.4% energy resolution for high-energy γ -rays. *Nature Photonics*, 15(1), 36-42.
- [65] Han, D., Zhang, T., Huang, M., Sun, D., Du, M. H., & Chen, S. (2018). Predicting the thermodynamic stability of double-perovskite halides from density functional theory. *APL Materials*, 6(8), 084902.
- [66] Ghasemi, M., Hao, M., Xiao, M., Chen, P., He, D., Zhang, Y., ... & Wen, X. (2020). Lead-free metal-halide double perovskites: from optoelectronic properties to applications. *Nanophotonics*.
- [67] Zhang, H., Dun, G., Feng, Q., Zhao, R., Liang, R., Gao, Z., ... & Ren, T. L. (2020). Encapsulated X-ray detector enabled by all-inorganic lead-free perovskite film with high sensitivity and low detection limit. *IEEE Transactions on Electron Devices*, 67(8), 3191-3198.
- [68] Keshavarz, M., Debroye, E., Ottesen, M., Martin, C., Zhang, H., Fron, E., ... & Hofkens, J. (2020). Tuning the Structural and Optoelectronic Properties of Cs₂AgBiBr₆ Double-Perovskite Single Crystals through Alkali-Metal Substitution. *Advanced Materials*, 32(40), 2001878.
- [69] Su, J., Huang, Y. Q., Chen, H., & Huang, J. (2020). Solution Growth and Performance Study of Cs₂AgBiBr₆ Single Crystal. *Crystal Research and Technology*, 55(3), 1900222.

- [70] Zhang, Y., Liu, Y., Xu, Z., Ye, H., Yang, Z., You, J., ... & Liu, S. F. (2020). Nucleation-controlled growth of superior lead-free perovskite Cs₃Bi₂I₉ single-crystals for high-performance X-ray detection. *Nature communications*, 11(1), 1-11.
- [71] Liu, Y., Zhang, Y., Yang, Z., Cui, J., Wu, H., Ren, X., ... & Liu, S. (2020). Large Lead-Free Perovskite Single Crystal for High-Performance Coplanar X-Ray Imaging Applications. *Advanced Optical Materials*, 8(19), 2000814.
- [72] Liu, Y., Xu, Z., Yang, Z., Zhang, Y., Cui, J., He, Y., ... & Liu, S. F. (2020). Inch-size 0D-structured lead-free perovskite single crystals for highly sensitive stable X-ray imaging. *Matter*, 3(1), 180-196.
- [73] Zheng, X., Zhao, W., Wang, P., Tan, H., Saidaminov, M. I., Tie, S., ... & Zhang, W. H. (2020). Ultrasensitive and stable X-ray detection using zero-dimensional lead-free perovskites. *Journal of Energy Chemistry*, 49, 299-306.
- [74] Tie, S., Zhao, W., Huang, W., Xin, D., Zhang, M., Yang, Z., ... & Zhang, W. H. (2020). Efficient X-ray attenuation lead-free AgBi₂I₇ halide ruddersite alternative for sensitive and stable X-ray detection. *The Journal of Physical Chemistry Letters*, 11(19), 7939-7945.
- [75] Steele, J. A., Pan, W., Martin, C., Keshavarz, M., Debroye, E., Yuan, H., ... & Roeffaers, M. B. (2018). Photophysical pathways in highly sensitive Cs₂AgBiBr₆ double-perovskite single-crystal X-ray detectors. *Advanced Materials*, 30(46), 1804450.
- [76] Yuan, W., Niu, G., Xian, Y., Wu, H., Wang, H., Yin, H., ... & Fan, J. (2019). In situ regulating the order-disorder phase transition in Cs₂AgBiBr₆ single crystal toward the application in an X-ray detector. *Advanced Functional Materials*, 29(20), 1900234.
- [77] Xu, Z., Liu, X., Li, Y., Liu, X., Yang, T., Ji, C., ... & Sun, Z. (2019). Exploring Lead-Free Hybrid Double Perovskite Crystals of (BA)₂CsAgBiBr₇ with Large Mobility-Lifetime

- Product toward X-Ray Detection. *Angewandte Chemie International Edition*, 58(44), 15757-15761.
- [78] Yin, L., Wu, H., Pan, W., Yang, B., Li, P., Luo, J., ... & Tang, J. (2019). Controlled cooling for synthesis of Cs₂AgBiBr₆ single crystals and its application for X-ray detection. *Advanced Optical Materials*, 7(19), 1900491.
- [79] Guo, W., Liu, X., Han, S., Liu, Y., Xu, Z., Hong, M., ... & Sun, Z. (2020). Room-Temperature Ferroelectric Material Composed of a Two-Dimensional Metal Halide Double Perovskite for X-ray Detection. *Angewandte Chemie*, 132(33), 13983-13988.
- [80] Xu, Z., Wu, H., Li, D., Wu, W., Li, L., & Luo, J. (2021). A lead-free I-based hybrid double perovskite (IC₄H₈NH₃)₄AgBiI₈ for X-ray detection. *Journal of Materials Chemistry C*, 9(38), 13157-13161.
- [81] Yakunin, S., Sytnyk, M., Kriegner, D., Shrestha, S., Richter, M., Matt, G. J., ... & Heiss, W. (2015). Detection of X-ray photons by solution-processed lead halide perovskites. *Nature photonics*, 9(7), 444-449.
- [82] Ighodalo, K. O., Chen, W., Liang, Z., Shi, Y., Chu, S., Zhang, Y., ... & Xiao, Z. (2023). Negligible Ion Migration in Tin-Based and Tin-Doped Perovskites. *Angewandte Chemie International Edition*, 62(5), e202213932.
- [83] Li, L., Liu, X., Zhang, H., Zhang, B., Jie, W., Sellin, P. J., ... & Xu, Y. (2019). Enhanced X-ray sensitivity of MAPbBr₃ detector by tailoring the interface-states density. *ACS applied materials & interfaces*, 11(7), 7522-7528.
- [84] Zhang, H., Gao, Z., Liang, R., Zheng, X., Geng, X., Zhao, Y., ... & Ren, T. L. (2019). X-ray detector based on all-inorganic lead-free Cs₂AgBiBr₆ perovskite single crystal. *IEEE Transactions on Electron Devices*, 66(5), 2224-2229.

- [85] Ralaifarisoa, M., Busby, Y., Frisch, J., Salzmann, I., Pireaux, J. J., & Koch, N. (2017). Correlation of annealing time with crystal structure, composition, and electronic properties of $\text{CH}_3\text{NH}_3\text{PbI}_{3-x}\text{Cl}_x$ mixed-halide perovskite films. *Physical Chemistry Chemical Physics*, *19*(1), 828-836.
- [86] Alghamdi, S., Bennett, S., Crean, C., Ghosh, J., Gibbard, H., Moss, R., ... & Sellin, P. (2022). Polycrystalline formamidinium lead bromide x-ray detectors. *Applied sciences*, *12*(4), 2013.
- [87] Yang, L., Zhang, H., Zhou, M., Zhao, L., Chen, W., Wang, T., ... & Xu, X. (2020). High-stable X-ray imaging from all-inorganic perovskite nanocrystals under a high dose radiation. *The Journal of Physical Chemistry Letters*, *11*(21), 9203-9209.
- [88] Lan, C., Liang, G., Zhao, S., Lan, H., Peng, H., Zhang, D., ... & Fan, P. (2019). Lead-free formamidinium bismuth perovskites (FA) $3\text{Bi}_2\text{I}_9$ with low bandgap for potential photovoltaic application. *Solar Energy*, *177*, 501-507.
- [89] National Institute of Standards and Technology Physical Meas. Laboratory, XCOM, <https://physics.nist.gov/PhysRefData/Xcom/html/xcom1.html>
- [90] Jiang, H., & Kloc, C. (2013). Single-crystal growth of organic semiconductors. *MRS bulletin*, *38*(1), 28-33.
- [91] Yu, J., Liu, G., Chen, C., Li, Y., Xu, M., Wang, T., ... & Zhang, L. (2020). Perovskite CsPbBr_3 crystals: growth and applications. *Journal of Materials Chemistry C*, *8*(19), 6326-6341.
- [92] Agrawal, K., Hasan, S. M. A., Blawat, J., Mehta, N., Wang, Y., Cueto, R., ... & Gartia, M. R. (2022). Thermal, Physical, and Optical Properties of the Solution and Melt Synthesized Single Crystal CsPbBr_3 Halide Perovskite. *Chemosensors*, *10*(9), 369.

- [93] Wei, H., DeSantis, D., Wei, W., Deng, Y., Guo, D., Savenije, T. J., ... & Huang, J. (2017). Dopant compensation in alloyed $\text{CH}_3\text{NH}_3\text{PbBr}_{3-x}\text{Cl}_x$ perovskite single crystals for gamma-ray spectroscopy. *Nature materials*, *16*(8), 826-833.
- [94] Jiang, Q., Zhao, Y., Zhang, X., Yang, X., Chen, Y., Chu, Z., ... & You, J. (2019). Surface passivation of perovskite film for efficient solar cells. *Nature Photonics*, *13*(7), 460-466.
- [95] Wu, C. Y., Wang, Z., Liang, L., Gui, T., Zhong, W., Du, R. C., ... & Luo, L. B. (2019). Graphene-Assisted Growth of Patterned Perovskite Films for Sensitive Light Detector and Optical Image Sensor Application. *Small*, *15*(19), 1900730.
- [96] Rakita, Y., Cohen, S. R., Kedem, N. K., Hodes, G., & Cahen, D. (2015). Mechanical properties of APbX_3 (A= Cs or CH_3NH_3 ; X= I or Br) perovskite single crystals. *Mrs Communications*, *5*(4), 623-629.
- [97] Cao, D., & Yang, G. (2022). Effect of low-temperature annealing on Bi-poor $\text{Cs}_2\text{AgBiBr}_6$ single crystals. *Materials Today Communications*, *33*, 104242.
- [98] Yan, W., Pun, C. L., & Simon, G. P. (2012). Conditions of applying Oliver–Pharr method to the nanoindentation of particles in composites. *Composites Science and Technology*, *72*(10), 1147-1152.
- [99] Makuła, P., Pacia, M., & Macyk, W. (2018). How to correctly determine the band gap energy of modified semiconductor photocatalysts based on UV–Vis spectra. *The journal of physical chemistry letters*, *9*(23), 6814-6817.
- [100] Chen, C., Song, Z., Xiao, C., Zhao, D., Shrestha, N., Li, C., ... & Yan, Y. (2019). Achieving a high open-circuit voltage in inverted wide-bandgap perovskite solar cells with a graded perovskite homojunction. *Nano Energy*, *61*, 141-147.

- [101] Ruan, S., McMeekin, D. P., Fan, R., Webster, N. A., Ebendorff-Heidepriem, H., Cheng, Y. B., ... & McNeill, C. R. (2020). Raman spectroscopy of formamidinium-based lead halide perovskite single crystals. *The Journal of Physical Chemistry C*, *124*(4), 2265-2272.
- [102] Zhang, L., Liu, C., Lin, Y., Wang, K., Ke, F., Liu, C., ... & Zou, B. (2019). Tuning optical and electronic properties in low-toxicity organic–inorganic hybrid (CH₃NH₃)₃Bi₂I₉ under high pressure. *The Journal of Physical Chemistry Letters*, *10*(8), 1676-1683.
- [103] Ruan, S., McMeekin, D. P., Fan, R., Webster, N. A., Ebendorff-Heidepriem, H., Cheng, Y. B., ... & McNeill, C. R. (2020). Raman spectroscopy of formamidinium-based lead halide perovskite single crystals. *The Journal of Physical Chemistry C*, *124*(4), 2265-2272.
- [104] Tsuboi, M., Komatsu, M., Hoshi, J., Kawashima, E., Sekine, T., Ishido, Y., ... & Thomas, G. J. (1997). Raman and infrared spectra of (2'-S)-[2'-2H] thymidine: Vibrational coupling between deoxyribosyl and thymine moieties and structural implications. *Journal of the American Chemical Society*, *119*(8), 2025-2032.
- [105] Hijazi, N., Panneerselvam, D., & Kabir, M. Z. (2018). Electron–hole pair creation energy in amorphous selenium for high energy photon excitation. *Journal of Materials Science: Materials in Electronics*, *29*(1), 486-490.
- [106] Chen, M., Dong, X., Chu, D., Jia, B., Zhang, X., Zhao, Z., ... & Liu, S. (2023). Interlayer-Spacing Engineering of Lead-Free Perovskite Single Crystal for High-Performance X-ray Imaging. *Advanced Materials*, 2211977.
- [107] Tailor, N. K., Ghosh, J., Afroz, M. A., Bennett, S., Chatterjee, M., Sellin, P., & Satapathi, S. (2022). Self-powered x-ray detection and imaging using Cs₂AgBiCl₆ lead-free double perovskite single crystal. *ACS Applied Electronic Materials*, *4*(9), 4530-4539.

- [108] Zhang, J., Li, A., Li, B., Yang, M., Hao, X., Wu, L., ... & Zhang, J. (2022). Top-seed solution-based growth of perovskite Cs₃Bi₂I₉ single crystal for high performance X-ray detection. *ACS Photonics*, 9(2), 641-651.
- [109] H. Zhang, G. Dun, Q. Feng, R. Zhao, R. Liang, Z. Gao and T. L. Ren, Encapsulated X-ray detector enabled by allinorganic lead-free perovskite film with high sensitivity and low detection limit, *IEEE Trans. Electron Devices*, 2020, 67(8), 3191–3198.
- [110] Tisdale, J. T., Yoho, M., Tsai, H., Shrestha, S., Fernando, K., Baldwin, J. K., ... & Nie, W. (2020). Methylammonium Lead Tribromide Single Crystal Detectors towards Robust Gamma-Ray Photon Sensing. *Advanced Optical Materials*, 8(10), 2000233.
- [111] Feng, Y., Pan, L., Wei, H., Liu, Y., Ni, Z., Zhao, J., ... & Huang, J. (2020). Low defects density CsPbBr₃ single crystals grown by an additive assisted method for gamma-ray detection. *Journal of Materials Chemistry C*, 8(33), 11360-11368.
- [112] Yang, B., Pan, W., Wu, H., Niu, G., Yuan, J. H., Xue, K. H., ... & Tang, J. (2019). Heteroepitaxial passivation of Cs₂AgBiBr₆ wafers with suppressed ionic migration for X-ray imaging. *Nature communications*, 10(1), 1989.

APPENDICES

Appendix A: Effect of Growth Seeded Solution Evaporation Growth Method

For solution evaporation growth method, it is crucial that controlling the nucleation energy to form a structure of perovskite, e.g., ABX_3 and $A_3B_2X_9$, because nucleation process is the starting point of single crystal growth. Generally, the transparent beaker was used to grow single crystals, so that the single crystals can be grown on the bottom of the beaker. Nucleation energy varies depending on the location of the bottom of the beaker, with lower nucleation energy observed in the peripheral regions adjacent to the surface of the beaker, while higher nucleation energy is observed in the central region of the beaker bottom. Thus, as shown in Figure A.1, which is the growth result of solution evaporation method without seed, many single crystals are closely packed together. This provides a challenging environment for the growth of a single, bulk crystal, because each single crystal infringes on the space of others.



Figure A.1 Growth result of $FA_3Bi_2I_9$ perovskite single crystals using solution evaporation method without seed.

On the other hand, the seeded solution evaporation method can significantly reduce nucleation energy, leading to minimal nucleation in areas other than the provided seed. As illustrated in Figure A.2, only the inserted seed grew into a bulk single crystal, while no single crystals were observed in other regions.



Figure A.2 Growth result of $\text{FA}_3\text{Bi}_2\text{I}_9$ perovskite single crystals using solution evaporation method with seed, whose size is approximately illustrated.

Appendix B: Estimation of Mobility-Lifetime ($\mu\tau$) Product

Predicting the mobility-lifetime ($\mu\tau$) product is significant in assessing how quickly and efficiently the charge carrier, electron and hole pairs, in semiconductors can move without being lost before reaching the electrodes. Therefore, a higher $\mu\tau$ product enables more effective radiation detection. The most commonly used method for predicting this product is using charge collection efficiency (CCE). Figure B.1 illustrates the results obtained by calculating CCE for each sample and fitting it to the modified Hecht equation.

Fitting results obtained for as-grown 80°C- and 120°C-annealed FA₃Bi₂I₉ hybrid perovskite single crystals were in good agreement with the measured CCE, resulting in the highest values for the $\mu\tau$ product. In contrast, 160°C-annealed single crystal showed a significant deviation between the fitted results and measured CCE, resulting in the lowest values for the $\mu\tau$ product. Therefore, it can be explained that temperature annealing at 80°C and 120°C provides optimal conditions for charge carriers to move efficiently due to the suppression of ion migration phenomena and improved surface conditions, which help for charge carriers to be transported to current collection system. On the other hand, temperature annealing at 160°C resulted in the formation of damage or defects in the perovskite internal structure, leading to a decrease in the $\mu\tau$ product.

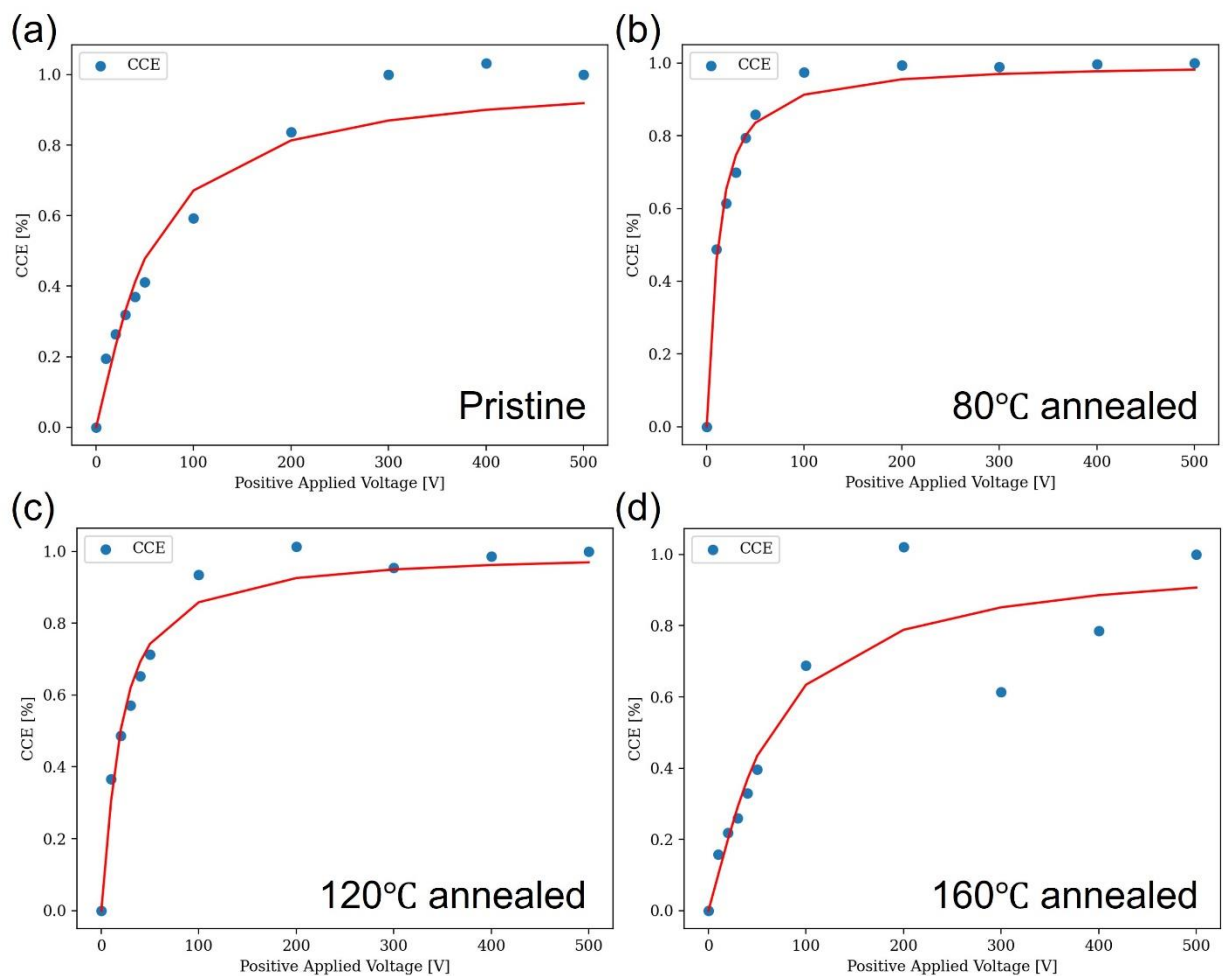


Figure B.1 Bias voltage dependent charge collection efficiency (CCE) estimation results of (a) pristine, (b) 80°C-, (c) 120°C-, and (d) 160°C-annealed FA₃Bi₂I₉ as-grown single crystals.

Appendix C: Stability under Long Time X-ray Exposure

To be a promising radiation detector material, it is crucial that the material produces consistent results over a long period of high energy adiation exposure. Therefore, as-grown $\text{FA}_3\text{Bi}_2\text{I}_9$ single crystals were also subjected to X-ray exposure for a prolonged time, and the photocurrent was analyzed. The results show that there is no significant change in performance after 30 minutes of X-ray exposure, for both the pristine and 120°C-annealed samples.

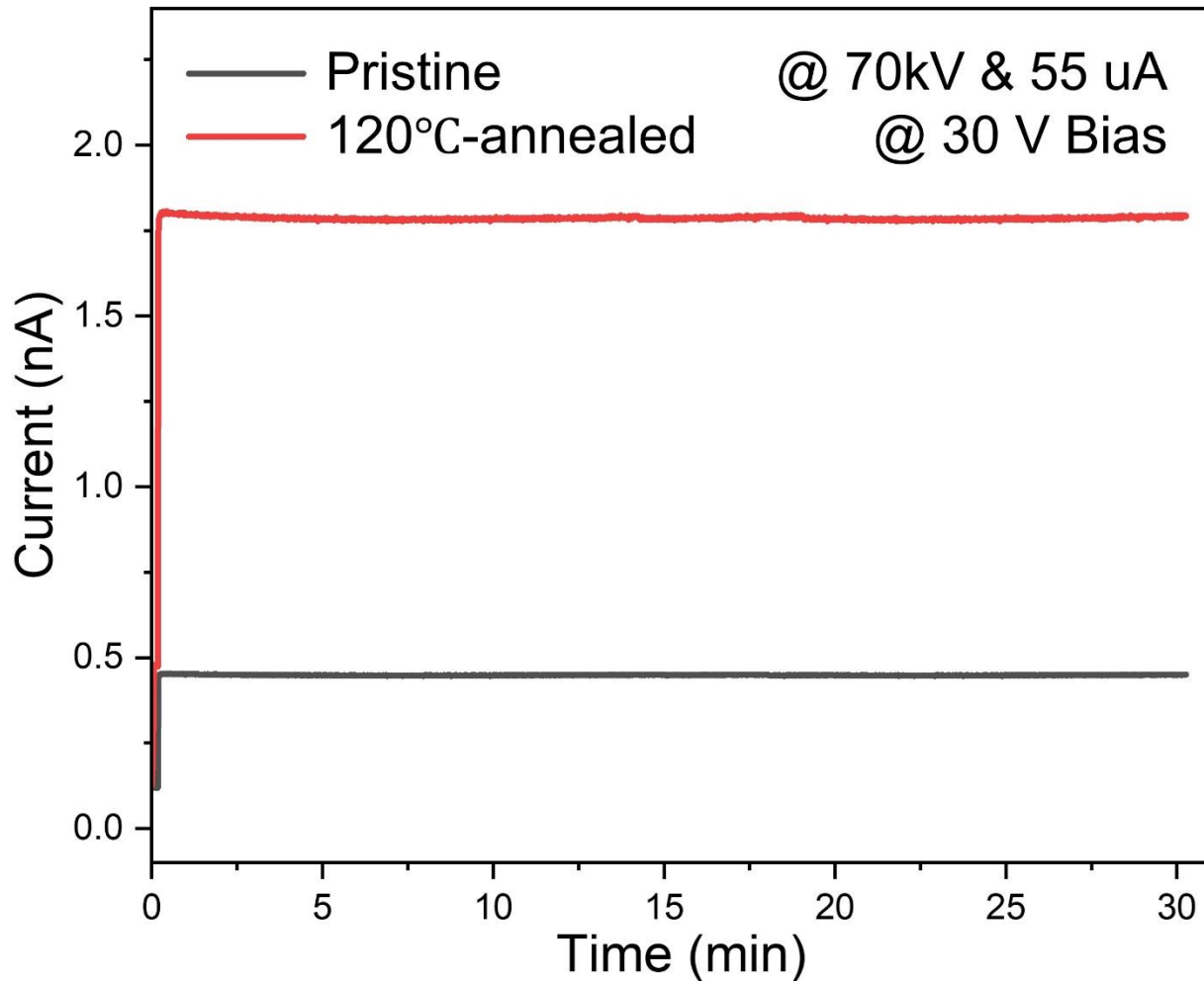


Figure C.1 Photocurrent measurement under X-ray dose rate of 6.78 Gy/s for 30 minutes using as-grown pristine and 120°C-annealed $\text{FA}_3\text{Bi}_2\text{I}_9$ single crystal.